Redshift-space distortions with the halo occupation distribution – I. Numerical simulations

Jeremy L. Tinker,[1][*][†] David H. Weinberg[1] and Zheng Zheng[2][‡]

[1]*Department of Astronomy, The Ohio State University, 140 W. 18th Avenue, Columbus, OH 43210, USA*
[2]*Institute for Advanced Study, School of Natural Sciences, Einstein Drive, Princeton, NJ 08540, USA*

ABSTRACT

We show how redshift-space distortions of the galaxy correlation function or power spectrum can constrain the matter density parameter Ω_m and the linear matter fluctuation amplitude σ_8. We improve on previous treatments by adopting a fully non-linear description of galaxy clustering and bias, which allows us to achieve the accuracy demanded by larger galaxy redshift surveys and to break parameter degeneracies by combining large-scale and small-scale distortions. Given an observationally motivated choice of the initial power spectrum shape, we consider different combinations of Ω_m and σ_8 and find parameters of the galaxy halo occupation distribution (HOD) that yield nearly identical galaxy correlation functions in real space. We use these HOD parameters to populate the dark matter haloes of large N-body simulations, from which we measure redshift-space distortions on small and large scales. We include a velocity bias parameter α_v that allows the velocity dispersions of satellite galaxies in haloes to be systematically higher or lower than those of dark matter. Large-scale distortions are determined by the parameter combination $\beta \equiv \Omega_m^{0.6}/b_g$, where b_g is the bias factor defined by the ratio of galaxy and matter correlation functions, in agreement with the linear theory prediction of parameter degeneracy. However, linear theory does not accurately describe the distortions themselves on scales accessible to our simulations. We provide fitting formulas to estimate β from measurements of the redshift-space correlation function or power spectrum, and we show that these formulas are significantly more accurate than those in the existing literature. On small scales, the 'FOG' distortions at projected separations $\sim 0.1\, h^{-1}$ Mpc depend on $\Omega_m \alpha_v^2$ but are independent of σ_8, while at intermediate separations they depend on σ_8 as well. One can thus use measurements of redshift-space distortions over a wide range of scales to separately determine Ω_m, σ_8, and α_v.

Key words: galaxies: clusters: general – cosmology: theory – large-scale structure of Universe.

1 INTRODUCTION

In a universe that obeys the cosmological principle, the clustering of galaxies is statistically isotropic. But in galaxy redshift surveys the distances to galaxies are inferred from redshifts, making the line of sight a preferred direction. Peculiar velocities produce anisotropy in redshift-space clustering on all scales. On small scales, the random motions of galaxies in virialized systems stretch groups and clusters into so-called 'fingers-of-god' (FOG). On large scales, coherent flows created by gravity compress overdense regions along the line of sight and stretch underdense regions correspondingly. Small- and large-scale distortions provide diagnostics for the matter density parameter Ω_m and the amplitude of mass fluctuations (Peebles 1976; Sargent & Turner 1977; Kaiser 1987). In this paper and its companion, we develop techniques for modelling redshift-space distortions that draw on recent developments in the theory of galaxy clustering. These techniques are designed to reach the level of accuracy demanded by the new generation of large galaxy redshift surveys, such as the two-degree Field Galaxy Redshift Survey (2dFGRS; Colless et al. 2001) and the Sloan Digital Sky Survey (SDSS; York et al. 2000).

In the linear theory model of Kaiser (1987), the relation of the anisotropic, redshift-space galaxy power spectrum $P_Z(k, \mu)$ to the isotropic, real-space galaxy power spectrum $P_R(k)$ is

$$P_Z(k, \mu) = P_R(k)(1 + \beta\mu^2)^2, \tag{1}$$

[*]E-mail: tinker@cfcp.uchicago.edu
[†]Present address: Kavli Insitute for Cosmological Physics, University of Chicago, Chicago, IL 60637, USA.
[‡]Hubble Fellow.

where μ is the cosine of the angle between the wavevector $\boldsymbol{k}$, and the line of sight. The amplitude of the distortion is determined by $\beta = \Omega_m^{0.6}/b_{lin}$, where the linear bias parameter $b_{lin} \equiv \delta_g/\delta_m$ is assumed to be independent of scale (δ_g and δ_m represent galaxy and mass density contrasts, respectively). Fourier transformation of equation (1) gives expressions for the galaxy correlation function in redshift space, $\xi(r_\sigma, r_\pi)$ (Hamilton 1998).

Unfortunately, non-linear effects make equation (1) inaccurate on all scales where observations yield precise measurements (Cole, Fisher & Weinberg 1994). The effects of non-linearity can be approximated by a phenomenological model in which galaxies have, in addition to linear theory distortions, random small-scale velocities drawn from an exponential distribution with dispersion σ_v (Park et al. 1994; Peacock & Dodds 1994; Cole, Fisher & Weinberg 1995). In this model, the Kaiser formula becomes

$$P_Z(k, \mu) = P_R(k)(1 + \beta \mu^2)^2 \left(1 + \frac{k^2 \sigma_v^2 \mu^2}{2}\right)^{-2}. \qquad (2)$$

In practice, most estimates of β from large-scale redshift-space distortions have utilized this linear–exponential model,[1] expressed in terms of the power spectrum as in equation (2) or in terms of the correlation function or spherical harmonics. The current state-of-the-art measurement is the analysis of the 2dFGRS presented by Hawkins et al. (2003), yielding $\beta = 0.49 \pm 0.09$, updating the earlier 2dFGRS analysis of Peacock et al. (2001). Previous observational efforts and theoretical developments are expertly reviewed by Strauss & Willick (1995) and Hamilton (1998).

The essential limitation of equation (2) is that it is derived from an unphysical model. There are several sources of non-linearity in redshift-space distortions in addition to small-scale dispersion (Cole et al. 1994; Fisher & Nusser 1996), and the dispersion itself is correlated with the local density and is not a constant for all galaxies. Scoccimarro (2004) shows that the velocity distribution corresponding to the linear–exponential model is itself unphysical, containing a δ-function and a discontinuity at the origin, and that equation (2) does not become fully accurate even at very large scales. Hatton & Cole (1999) concluded that this model introduces a $\sim$15 per cent systematic error in the determination of β, which is significant compared to the precision achievable with 2dFGRS and the SDSS. Furthermore, the σ_v parameter, while related to the amplitude of the small-scale distortions, has no clearly defined physical meaning. In redshift-space distortion analyses it is purely a nuisance parameter, significantly degenerate with β, and has no use in constraining cosmological parameters.

The program initiated by Kaiser (1987) largely supplanted an earlier tradition of using small-scale redshift distortions to constrain Ω_m via the 'cosmic virial theorem' (Peebles 1976; Davis, Geller & Huchra 1978; Peebles 1979; Bean et al. 1983). The analytic expression of this 'theorem' relied on the assumption of stable clustering, which early N-body simulations showed was unlikely to hold on the relevant scales (e.g. Davis et al. 1985). A more serious problem is that the bias between galaxy and dark matter clustering is likely to have a complex effect on quantities that enter the cosmic virial theorem, one that cannot be captured by a single bias parameter with an obvious physical interpretation.

The goal of this paper and its companion is to present techniques for physical modelling of redshift-space distortions that can take ad-

---

[1] There are several minor variants of this model that have also been utilized, such as replacing the exponential distribution with a Gaussian (Peacock & Dodds 1994) or specifying that the pairwise distribution of galaxy peculiar velocities is exponential (e.g. Hatton & Cole 1999).

vantage of high-precision measurements on large and small scales. We construct these techniques in the framework of the halo occupation distribution (HOD; see e.g. Ma & Fry 2000; Peacock & Smith 2000; Seljak 2000; Benson 2001; Scoccimarro et al. 2001; Berlind & Weinberg 2002; Cooray & Sheth 2002), in which the bias of a specified class of galaxies is defined by the probability distribution $P(N|M)$ that a halo of mass M contains N galaxies, together with prescriptions for spatial and velocity bias within individual haloes. The HOD has proven to be a powerful tool for encapsulating the bias predictions of galaxy formation models (Kauffmann, Nusser & Steinmetz 1997; Benson et al. 2000; White, Hernquist & Springel 2001; Yoshikawa et al. 2001; Berlind et al. 2003; Kravtsov et al. 2004; Zheng et al. 2004), for analytic calculations of galaxy clustering statistics (see Cooray & Sheth 2002 and numerous references therein), and for empirical modelling of galaxy clustering data (Jing, Mo & Börner 1998; Magliocchette & Porciani 2003; van den Bosch, Yang & Mo 2003; Zehavi et al. 2004, 2005; Abazajian et al. 2005; Mo, Yang & van den Bosch 2004; Tinker et al. 2005; Yang et al. 2004; Collister & Lahav 2005). Several recent papers have presented calculations of redshift-space distortions or peculiar velocity statistics using halo models of dark matter and galaxy clustering (Seljak 2001; Sheth et al. 2001; Sheth & Diaferio 2001; White 2001; Kang et al. 2002; Cooray 2004), providing insight into the role of non-linear dynamics and non-linear bias in shaping clustering and anisotropy. However, these studies primarily focus on dark matter rather than galaxy clustering, and they have not yet yielded a clear blueprint for constraining cosmological parameters with HOD modelling of observed redshift-space distortions, which is our objective here.

We use the HOD formulation to set up the redshift-space distortion problem in the following terms. Any redshift survey large enough to yield useful measurements of large-scale anisotropy will first allow precise measurements of the projected correlation function, $w_p(r_p)$, which is unaffected by peculiar velocities. For any choice of cosmological parameters, one should choose HOD parameters to reproduce this measurement of real-space clustering. If an acceptable fit cannot be found for the given cosmology, then the model is already ruled out (e.g. Abazajian et al. 2005). For models with acceptable real-space clustering, one calculates redshift-space distortions using numerical simulations or analytic approximations to test the cosmological parameters of the model. In practice, the parameters that enter are Ω_m and the amplitude of the linear theory matter power spectrum $P_{lin}(k)$, which we characterize by σ_8, the rms linear matter fluctuation in $8\,h^{-1}$ Mpc spheres (with $h \equiv H_0/100\,\mathrm{km\,s^{-1}\,Mpc^{-1}}$). We assume that the *shape* of $P_{lin}(k)$ is known from measurements of the large-scale galaxy power spectrum and cosmic microwave background (CMB) anisotropy, which together pin down the parameters that determine $P_{lin}(k)$ quite accurately (e.g. Percival et al. 2002; Spergel et al. 2003; Tegmark et al. 2004a). Since redshift-space anisotropy is insensitive to the shape of $P_R(k)$ – in equations (1) and (2) the μ-dependence of $P_Z(k)$ factors out entirely – small uncertainties in the shape of $P_{lin}(k)$ should have minimal effect. In this work we adopt the power spectrum form of Efstathiou, Bond & White (1992), where the shape is parametrized by the characteristic wavenumber Γ.

While matching $w_p(r_p)$ can constrain HOD parameters relevant to real-space clustering, we must also allow for the possibility that galaxies in a halo have a systematically different velocity dispersion from that of the halo dark matter. (The mean velocity of galaxies and dark matter within a halo should be the same because both components feel the same large-scale gravitational field.) Numerical simulations predict that the galaxy closest to the halo

centre of mass moves at nearly the centre of mass velocity while satellite galaxies and dark matter subhaloes have a velocity dispersion similar to that of the dark matter (Klypin et al. 1999; Ghigna et al. 2000; Springel et al. 2001; Berlind et al. 2003; Diemand, Moore & Stadel 2004; Faltenbacher et al. 2005). We define the satellite 'velocity bias', α_v, as the ratio between these two dispersions. Although the numerical simulations predict that $\alpha_v \approx 1$, this parameter could depart modestly from unity as a result of dynamical friction, tidal disruption or mergers of slowly moving satellites, or different orbital anisotropy of galaxies and dark matter. We will treat α_v as a free parameter to be constrained by the observations, but we will assume that it is constant over the relevant range of halo masses. We will also consider effects of non-zero velocities for central galaxies, though simulations predict these velocities to be $\lesssim 20$ per cent of the virial velocity.

In this paper we use N-body simulations to create halo populations for a set of cosmological models, and we populate those haloes with galaxies using HOD models that yield similar real-space clustering. We examine the constraints that redshift-space distortions can impose within the three-dimensional parameter space (Ω_m, σ_8, α_v), and we use our numerical results to obtain fitting formulas that can estimate parameters from observational data. In a companion paper, we develop a numerically calibrated analytic model for redshift-space distortions. The analytic model provides physical insight into the numerical results, and it can make more complete use of the observational measurements for cosmological parameter estimation.

In Section 2, we describe the numerical simulations and the HOD models used to populate them with galaxies. Section 3 presents an overview of redshift-space anisotropies in the two-dimensional correlation function $\xi(r_\sigma, r_\pi)$. In Section 4, we focus on measures of large-scale distortion based on multipole decomposition of the power spectrum and the correlation function. These measures mainly constrain the parameter combination $\beta \equiv \Omega_m^{0.6}/b_g$, which can be related to $\sigma_8 \Omega_m^{0.6}$ using the measured (real-space) galaxy clustering. (As discussed in Section 4.4, we define b_g by a ratio of non-linear correlation functions, which makes it similar but not identical to the linear theory bias factor b_{lin}.) In Section 5 we turn to small-scale distortions, which most directly constrain $\Omega_m \alpha_v^2$ and have some power to break degeneracies further and yield separate determinations of Ω_m, σ_8 and α_v. In Section 6, we summarize our results and discuss how they can be applied to cosmological parameter estimation from observational data.

2 NUMERICAL SIMULATIONS AND HOD MODELS

2.1 *N-body simulations*

We use N-body simulations to create halo populations for a sequence of cosmological models, always assuming a spatially flat universe dominated by cold dark matter and a cosmological constant [Lambda cold dark matter (ΛCDM)], with Gaussian initial conditions and a primordial power spectrum motivated by observations of CMB anisotropies and large-scale structure.

We choose the mass resolution by requiring that there be at least 30 particles in the lowest mass haloes that host simulated galaxies. On this basis, we select a mean interparticle separation of $\bar{n}^{-1/3} = 0.7 \, h^{-1}$ Mpc for all initial conditions. For $\Omega_m = 0.3$, the 30-particle limit corresponds to a minimum halo mass of $\sim 10^{12} \, h^{-1}$ M$_\odot$, similar to the minimum halo mass found for the HOD fit (assuming $\Omega_m = 0.3$) to the SDSS sample of galaxies brighter than $M_r = -20 +$

5 log h (Zehavi et al. 2005). All of our simulated galaxy populations have a space density of $\bar{n}_g = 5.6 \times 10^{-3} \, (h^{-1}$ Mpc$)^{-3}$, equal to that of SDSS galaxies brighter than $0.68 \, L_*$ (Blanton et al. 2003), or $M_r = -20.04 + 5 \log h$.

To cover the (Ω_m, σ_8) parameter space in an efficient manner, we draw on the findings of Zheng et al. (2002), who demonstrated that changes in Ω_m at fixed Γ and σ_8 simply scale halo masses in proportion to Ω_m and halo velocities in proportion to $\Omega_m^{0.6}$. In terms of these scaled masses and velocities, the mass function, spatial correlations and velocity correlations of haloes identified at fixed overdensity are virtually independent of Ω_m. We can therefore run a single simulation that has a high value of σ_8 at redshift zero and use the earlier redshift outputs to represent $z = 0$ results for lower values of σ_8. For each σ_8, the halo population can be scaled to any desired value of Ω_m. Specifically, we run simulations with $\Omega_m = 0.1$ and $\sigma_8 = 0.95$ at $z = 0$, and use the outputs at $z = 0.19, 0.56, 0.97$ and 1.45 when $(\Omega_m, \sigma_8) = (0.16, 0.90), (0.30, 0.80), (0.46, 0.70)$ and $(0.62, 0.60)$. We model different values of Ω_m by scaling the halo masses in proportion to Ω_m, the halo velocities by $\Omega_m^{0.6}$ and the internal halo velocity dispersions by $\Omega_m^{0.5}$. We carry out a test of this scaling in Section 2.3 to demonstrate that it is accurate enough for our purposes here.

We analyse simulations with two values of the power spectrum shape parameter, $\Gamma = 0.2$ and 0.12, both with inflationary spectral index $n_s = 1$. On the scales probed by our simulations, $\Gamma = 0.2$ corresponds well to the power spectrum calculated with CMBFAST (Seljak & Zaldarriaga 1996) with $\Omega_m = 0.3, h = 0.7$ and $\Omega_b = 0.04$, values favoured by recent observations (e.g. Spergel et al. 2003; Tegmark et al. 2004b). The redder, $\Gamma = 0.12$ power spectrum corresponds to a lower combination of $\Omega_m h$, or a tilted ($n_s < 1$) primordial spectrum. This model is at the extreme edge of those allowed by current data, so comparing results for $\Gamma = 0.2$ and $\Gamma = 0.12$ should give a conservative estimate of uncertainties associated
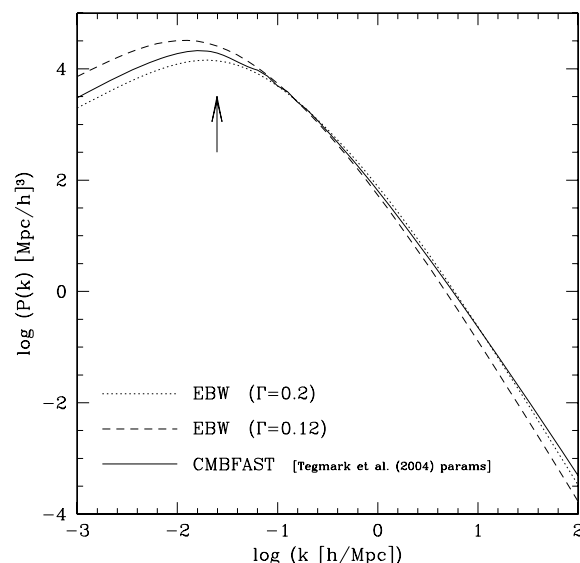

Figure 1. The two power spectra used in the simulations, $\Gamma = 0.2$ and 0.12, are compared to the linear power spectrum computed with CMBFAST using the parameters listed in column 6 of table 4 in Tegmark et al. (2004b). All three power spectra are normalized to the same value of σ_8. The fundamental mode of the simulation volume is indicated with the arrow at $k = 2\pi/L_{box} = 0.025 \, h$ Mpc^{-1}. The $\Gamma = 0.2$ power spectrum is similar to the CMBFAST calculation over the range of scales simulated, while the $\Gamma = 0.12$ power spectrum has more power at large scales and increasingly less as k increases.

with the power spectrum shape. In Fig. 1, we compare these two power spectra to one created with the transfer function calculated by CMBFAST using the cosmological parameters listed in table 4 (column 6) of Tegmark et al. (2004b), who derive combined constraints from *Wilkinson Microwave Anisotropy Probe* CMB data, and the SDSS galaxy power spectrum. Each power spectrum is normalized to the same value of σ_8. The fundamental mode of the box is marked with the arrow. Inside this scale, the $\Gamma = 0.2$ power spectrum closely tracks the CMBFAST calculation. The $\Gamma = 0.12$ $P(k)$ has less small-scale power, but it has significantly more power at scales near the fundamental mode.

In the inflationary CDM paradigm, the power spectrum shape depends on Ω_m, in addition to other parameters such as h, Ω_b, the spectral index n_s and its scale dependence, and neutrino masses. By adopting a fixed Γ, as we change Ω_m, we are implicitly assuming that other parameters are varying to approximately maintain the shape of $P_{lin}(k)$ as Ω_m changes, with h having the most leverage. Because observations constrain the shape of $P_{lin}(k)$ quite well, we consider the strategy better motivated than the alternative of changing $P_{lin}(k)$ with Ω_m, and it has the practical advantage of allowing one simulation to represent many Ω_m values. However, out diagnostics of σ_8 and Ω_m rely on the anisotropy of $P_z(k, \mu)$, not the shape of $P_{lin}(k)$, so we think that changing Γ in concert with Ω_m would lead to similar results.

We use the publicly available tree-code GADGET (Springel, Yoshida & White 2001) to integrate the initial conditions. We evolve 360^3 particles in a volume $253\,h^{-1}$ Mpc on a side, giving us a mass resolution of $9.66 \times 10^{10} \times \Omega_m\,h^{-1}\,M_\odot$ per particle. The force softening was set to 1/10th the mean interparticle separation, or $\epsilon = 70\,h^{-1}$ kpc. The simulations were started at an expansion factor $a = 0.01$, with a maximum time-step of 0.005 in a. GADGET employs individual particle time-steps governed by a particle's acceleration, such that $\Delta a \propto \sqrt{\epsilon\eta}$. The value of η was set to 0.2. We ran five independent realizations to estimate the sample variance. The SDSS reaches a limiting redshift of 0.1 for $M_r < -20 + 5 \log h$, so *one* of our simulations is roughly 70 per cent of the volume of the final SDSS sample (assuming it covers 8000 deg^2).

We also ran a similar series of simulations using the particle–mesh (PM) technique, with a staggered-mesh algorithm similar to that of Melott (1983) and Park (1990). (The code we use was written by V. Narayanan.) The high efficiency of the PM algorithm allowed us to run simulations with the same mass resolution but box sizes of $324\,h^{-1}$ Mpc per side, twice the volume of our GADGET runs. In comparing the results from the two methods, we found that the lower-force resolution of the PM technique (with a 900^3 grid) had a significant impact on the number of haloes near our 30-particle resolution limit, while the smaller volume of the GADGET runs did not adversely affect the distortions at large scales. We therefore use the GADGET runs exclusively in our subsequent analyses.

2.2 HOD models

To identify haloes in the dark matter distribution we use the friends-of-friends algorithm (Davis et al. 1985) with a linking length of 0.2 times the mean interparticle separation. Objects identified with this linking length typically have an average density of $\rho/\bar{\rho} \sim 200$, which is roughly the criterion for virialization of a collapsed object. Only haloes with 30 or more particles were retained in the halo sample.

We need to populate the haloes with galaxies in a way that generates similar $\xi_R(r)$ for all values of σ_8. We use the HOD parametrization of Kravtsov et al. (2004) and Zheng et al. (2004), which was
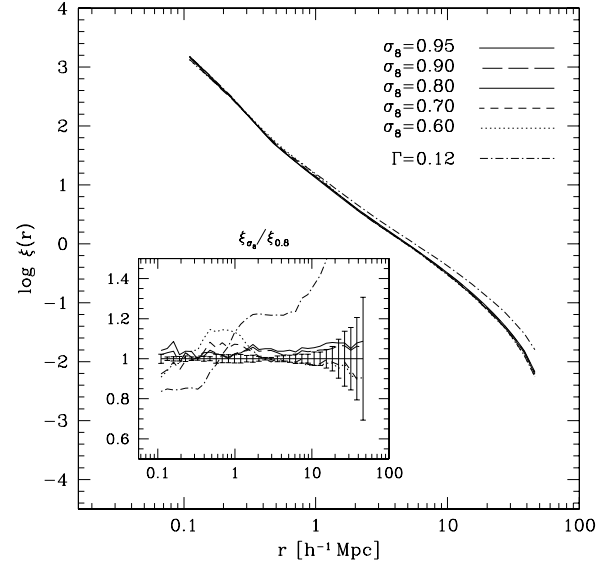

Figure 2. The real-space galaxy two-point correlation functions for the five cosmologies and HOD parameters listed in Table 1. The inset box shows the different correlation functions normalized by that of the central model, $\Omega_m = 0.3, \sigma_8 = 0.8$. The error bars in the inset box are those for the central model. Results are averaged over five realizations, and error bars show the run-to-run dispersion divided by $\sqrt{N-1} = 2$ to calculate the error in the mean. In both panels, the dash–dotted line is the correlation function for the central model's cosmological and HOD parameters for the $\Gamma = 0.12$ initial power spectrum.

also adopted in the empirical modelling of the SDSS correlation function by Zehavi et al. (2005). Haloes above a minimum mass M_{min} are assigned one central galaxy. The mean number of satellite galaxies in haloes with $M \geqslant M_{min}$ is

$$\langle N_{sat} \rangle_M = \left(\frac{M}{M_1} \right)^\alpha. \tag{3}$$

The mean number of galaxies in a halo is therefore $\langle N \rangle_M = 1 + (M/M_1)^\alpha$ for $M \geqslant M_{min}$ and $\langle N \rangle_M = 0$ for $M < M_{min}$. We assume Poisson scatter in the number of satellite galaxies with respect to the mean $\langle N_{sat} \rangle_M$, consistent with the theoretical predictions of Kravtsov et al. (2004) and Zheng et al. (2004).

We adopt the parameter combination $(\Omega_m, \sigma_8) = (0.3, 0.8)$ as our 'central' model, and we vary the cosmological parameters around these values. To populate the haloes in the central model, we choose observationally motivated HOD parameters similar to those derived for the SDSS $M_r < -20 + 5 \log h$ galaxy sample by Zehavi et al. (2005). The resulting correlation function is shown by the solid line in Fig. 2. For other σ_8 values, we choose M_1, α and M_{min} so that we closely match $\xi_R(r)$ of the central model, while maintaining a fixed galaxy space density. We carry out the HOD parameter fits using the analytic model of $\xi_R(r)$ described by Tinker et al. (2005), which refines the model described by Zheng (2004). The cosmological and HOD parameters of our simulations are listed in Table 1.

We assume that satellite galaxies trace the dark matter distribution within haloes; a test in Section 3 below shows that our results are insensitive to this assumption (see Fig. 7). Instead of selecting random dark matter particles from the friends-of-friends haloes, we randomly place satellite galaxies in each halo following the universal halo profile of Navarro, Frenk & White (1997; hereafter NFW). This technique makes our results insensitive to numerical force resolution or to discreteness effects on halo structure and velocity dispersions.

Table 1. Properties of the Simulations and HOD Parameters.

z_{out}	Ω_{m}	σ_8	b_{g}	M_{min} ($h^{-1}\,\mathrm{M}_{\odot}$)	M_1 ($h^{-1}\,\mathrm{M}_{\odot}$)	α
0	0.100	0.950	0.922	3.73×10^{11}	9.38×10^{12}	0.934
0.19	0.158	0.900	0.956	5.96×10^{11}	1.45×10^{13}	0.959
0.56	0.297	0.801	1.041	1.09×10^{12}	2.51×10^{13}	1.005
0.97	0.459	0.699	1.181	1.70×10^{12}	3.51×10^{13}	1.109
1.45	0.620	0.599	1.358	2.19×10^{12}	3.99×10^{13}	1.199

Note. When we scale an output to a different value of Ω_{m}, the values of M_{min} and M_1 scale in proportion to Ω_{m}, as discussed in Section 2.3. The value of σ_8 in column 3 is the value predicted from linear theory. The galaxy bias in column 4 is determined from the ratio of galaxy and dark matter correlation functions in the simulations, $b_{\mathrm{g}}^2 = \xi_{\mathrm{g}}/\xi_{\mathrm{m}}$, averaged over the range $4 \leqslant r \leqslant 12\,h^{-1}$ Mpc.

It also allows for easier comparison to analytic approximations, since the N-body halo population is better controlled and characterized. Most importantly for our purposes, it allows us to choose halo concentrations appropriate to each combination of σ_8 and Ω_{m}, using the methods of Bullock et al. (2001) and Kuhlen et al. (2005).[2] The simple scaling of halo properties found by Zheng et al. (2002) does not extend to internal structure, which depends systematically on Ω_{m}. When creating galaxy populations for models with different Ω_{m} but the same σ_8, we change halo concentrations appropriately and scale the values of M_1 and M_{min} with Ω_{m}. This procedure leads to small differences in $\xi_R(r)$ from model to model, but these have negligible impact on our redshift-space distortion results. We discuss concentration effects at the end of Section 3.

We draw line-of-sight velocities of satellite galaxies (relative to the halo centre-of-mass) from a Gaussian distribution with dispersion

$$\sigma_{\mathrm{v}}(M) = \alpha_{\mathrm{v}} \left(\frac{GM}{2R_{200}} \right)^{1/2}, \qquad (4)$$

where R_{200} is the radius at which the mean density of the halo is 200 times the background density $\bar{\rho}$. For $\alpha_{\mathrm{v}} = 1$, this choice corresponds to the velocity distribution of an isothermal sphere. Although a literal interpretation of $\alpha_{\mathrm{v}} \neq 1$ is that the satellite population is 'colder' or 'hotter' than the dark matter particles, a modest departure from unity can also account for orbital anisotropy and non-isothermality. For a halo with an NFW density profile, the mean velocity dispersion given by the Jeans equation (cf. van den Bosch et al. 2004; equation 7) deviates slightly from that of equation (4). We discuss the effects of anisotropy non-isothermality in Section 5 below, and demonstrate that these effects can be well described by a simple velocity bias parameter.

We use a similar technique for the velocities of central galaxies, but here our standard assumption is that the velocity bias parameter $\alpha_{\mathrm{vc}} = 0$. We also consider a model in which the central galaxies have modest velocities, $\alpha_{\mathrm{vc}} = 0.2$, and an extreme model with $\alpha_{\mathrm{vc}} = 1$. We also consider models with *satellite* $\alpha_{\mathrm{v}} = 0$ to isolate the physical effects of the virial dispersion from those of the halo velocities. The $\alpha_{\mathrm{v}} = 0$ models are also relevant to observational analyses that

employ 'FOG compression', i.e. identification and compression of galaxy groups in redshift space (see e.g. Tegmark et al. 2004a). If this technique works perfectly, it effectively sets $\alpha_{\mathrm{v}} = 0$ in all haloes.

Fig. 2 shows real-space galaxy correlation functions for $\Gamma = 0.2$ and $\sigma_8 = 0.6, 0.7, 0.8, 0.9$ and 0.95 (see Table 1 for exact values). Results are averaged over five realizations, and error bars show the run-to-run dispersion divided by $\sqrt{N-1} = 2$ to yield the error in the mean. The inset box shows the deviation of $\xi_R(r)$ for each model relative to that of the central ($\Omega_{\mathrm{m}} = 0.3, \sigma_8 = 0.8$) model. The models with $\sigma_8 \geqslant 0.7$ match the central model to $\lesssim 5$ per cent at $r \lesssim 20\,h^{-1}$ Mpc. At larger scales, finite box effects make the deviations larger than 10 per cent, but these are smaller than the statistical errors. The $\sigma_8 = 0.6$ model matches the central model to 5 per cent or better at most r, but it deviates by ~ 15 per cent around $0.8\,h^{-1}$ Mpc. At roughly this scale there is a transition between one- and two-halo galaxy pairs, and the effects of σ_8 on the halo mass function are difficult to overcome with $P(N|M)$ changes.

The dot–dashed curve in Fig. 2 shows $\xi_R(r)$ for the $\Omega_{\mathrm{m}} = 0.3, \sigma_8 = 0.8, \Gamma = 0.12$ model. With this large change in the shape of the matter power spectrum, it is impossible to choose HOD parameters that make the galaxy correlation function match that of the $\Gamma = 0.2$ models, or the SDSS data (Abazajian et al. 2005). Instead, for this set of models we use the same HOD parameters found for the corresponding σ_8 value in the $\Gamma = 0.2$ runs. The spread among $\xi_R(r)$ for the five $\Gamma = 0.12$ models is comparable to that for the $\Gamma = 0.2$ models. At $r < 2\,h^{-1}$ Mpc, however, the spread is approximately twice as large.

2.3 Velocity scaling

Fig. 3 tests the efficacy of the mass/velocity scaling technique described in Section 2.1. For this test, we ran two new sets of GADGET runs, each set comprised of five simulations with 200^3 particles in a $200\,h^{-1}$ Mpc box. One set has $(\Omega_{\mathrm{m}}, \sigma_8) = (0.1, 0.8)$ at $z = 0$, the other has $(\Omega_{\mathrm{m}}, \sigma_8) = (0.4, 0.8)$ at $z = 0$. In both cases we chose HOD parameters M_{min} and M_1 corresponding to 30 and 600 particles, respectively, with satellite occupation slope $\alpha = 1$.

Panel (a) of Fig. 3 shows contours of the redshift-space correlation function, $\xi(r_\sigma, r_\pi)$, where r_σ represents the projected separation between two galaxies and r_π the line-of-sight separation. This way of representing the data is widely used in observational studies, such as Peacock et al. (2001) and Hawkins et al. (2003); the relatively larger bin size used here noticeably affects the shape of the innermost contours. We use the distant observer approximation, so r_π simply becomes the redshift distance between galaxy pairs along one dimension of the box, accounting for the periodic boundary condition. Here, correlation functions are averaged over three projections of

---

[2] We use the Bullock et al. (2001) method of calculating $c_{\mathrm{vir}} = R_{\mathrm{vir}}/r_{\mathrm{s}}$, where R_{vir} is the virial radius of the halo and r_{s} is the NFW scale radius. The virial overdensity used by Bullock et al. (2001) depends on Ω_{m} and can be significantly different from the $200\bar{\rho}$ assumed here. To correct for this, we calculate c_{vir} for a given halo mass M_{vir}, then calculate the corresponding M_{200} (since the halo mass depends on the defined edge of the halo) and scale the concentration by R_{200}/R_{vir}. See Hu & Kravtsov (2003) for details.
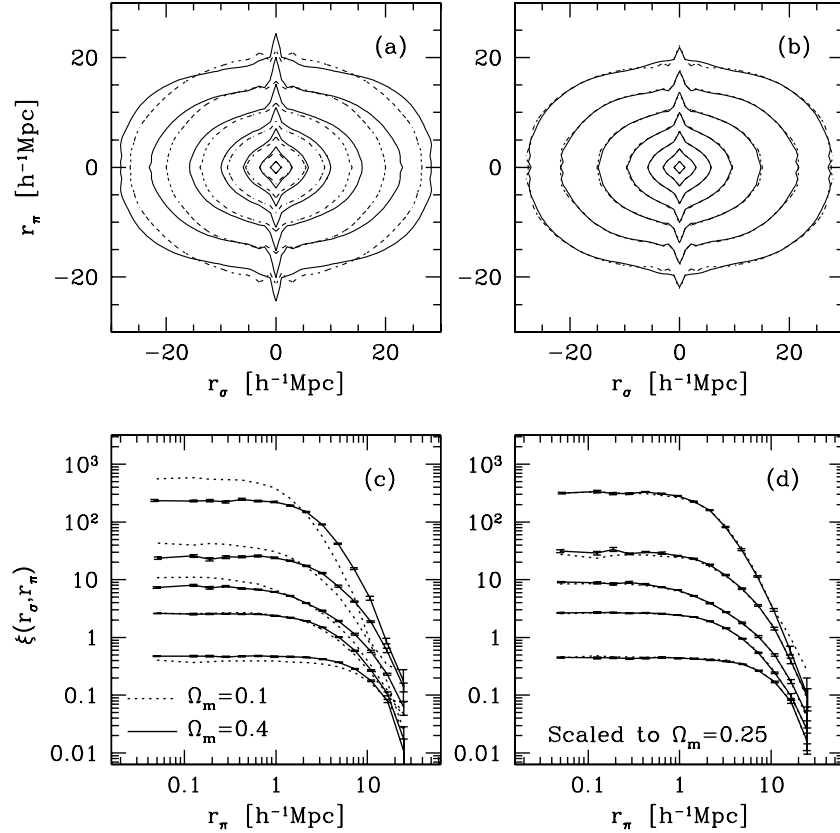
Figure 3. Test of the Ω_m-scaling procedure. For this test, we use simulations with 200^3 particles in a 200-h^{-1} Mpc box and HOD parameters $\alpha = 1$ and M_{min} and M_1 corresponding to 30 and 600 particles, respectively. (a) The correlation function in redshift space, $\xi(r_\sigma, r_\pi)$, for $\Omega_m = 0.1$ (dotted) and $\Omega_m = 0.4$ (solid). The contours represent lines of constant correlation separated by factors of 2, with the outermost contour representing 2^{-4}. (b) $\xi(r_\sigma, r_\pi)$ for the same models, but now the galaxy velocities have been scaled to $\Omega_m = 0.25$. (c) Same models as (a), but now the different lines represent slices in the $r_\sigma - r_\pi$ plane at different r_σ: 0.12, 0.3, 1, 3 and 11 h^{-1} Mpc from top to bottom. (d) The results from the two simulation sets, scaled to $\Omega_m = 0.25$, are plotted for the same slices in the $r_\sigma - r_\pi$ plane. Results in all panels are averaged over three projections of five realizations, and error bars in (c) and (d) show the run-to-run dispersion divided by $\sqrt{N-1} = \sqrt{14}$ to calculate the error in the mean. Errors are only plotted for the solid lines to avoid crowding.

five realizations for a total of 15 measurements. The higher density, $\Omega_m = 0.4$ model shows stronger compression of contours at large scales because of larger coherent flows, and it shows stronger FOG distortions at small scales because of larger dispersions between and within haloes.

Panel (c) presents the same data in a different fashion. Each line in the panel represents the value of $\xi(r_\sigma, r_\pi)$ as a function of r_π at a given r_σ, a slice in the $r_\sigma - r_\pi$ plane. At $r_\sigma = 0.12\,h^{-1}$ Mpc, the $\Omega_m = 0.4$ model starts at a lower value of $\xi(r_\sigma, r_\pi)$ but remains horizontal for a longer range of r_π. The extended horizontal plateau reflects the longer FOGs in the higher-density model, and since the pairs at small r_σ are spread over a larger range of r_π, the amplitude near $r_\pi = 0$ is necessarily depressed. We will use the turnover of $\xi(r_\pi)$ at small r_σ as a quantitative measure of small-scale distortions in Section 5. At the bottom of panel (c), where the lines represent $r_\sigma = 11\,h^{-1}$ Mpc, the $\Omega_m = 0.4$ line is above the $\Omega_m = 0.1$ line because of the large amplification of clustering in the coherent infalling regime.

In the right-hand panels, (b) and (d), we have scaled the velocities of the halo and galaxy populations of both models to $\Omega_m = 0.25$ in the manner described in Section 2.1, keeping HOD parameters fixed in *particle number* (and thus scaled in mass proportional to Ω_m). In both manners of representing the data, the correlation functions are nearly indistinguishable. In other words, we can scale an $\Omega_m = 0.1$ model to $\Omega_m = 0.25$ and 0.4 model to $\Omega_m = 0.25$ model and get the

same result. Fig. 3 demonstrates that our velocity scaling technique can be applied to our simulations without accruing systematic errors at either large or small scales.

3 OVERVIEW OF $\xi(r_\sigma, r_\pi)$

Fig. 4 encapsulates the dependence of the redshift-space correlation function, $\xi(r_\sigma, r_\pi)$, on position in the $(\Omega_m, \sigma_8, \alpha_v)$ parameter space. Each panel shows contours of $\xi(r_\sigma, r_\pi)$, separated by factors of 2, for a sequence of models in which two parameters or parameter combinations are held fixed and one is allowed to vary. Recall that these variations in cosmological parameters or velocity bias are carried out at fixed (or nearly fixed) *real-space* galaxy clustering, as shown in Fig. 2. The green contours in each panel of Fig. 4 show the central model with $\Omega_m = 0.3, \sigma_8 = 0.8, \alpha_v = 1.0, \alpha_{vc} = 0$, and all models have $\Gamma = 0.2$.

In panel (a), blue and red contours show models with $\sigma_8 = 0.6$ and 0.95, respectively, still with $\Omega_m = 0.3$ and $\alpha_v = 1$. As σ_8 increases, $\xi(r_\sigma, r_\pi)$ contours become more flattened because the amplitude of coherent flows increases with larger dark matter fluctuations. In terms of equation (1), higher σ_8 means a lower galaxy bias factor for fixed galaxy clustering amplitude, and thus a higher value of $\beta = \Omega_m^{0.6}/b_g$. In the FOG regime at small r_σ, contours of the three models are nearly degenerate at $r_\pi \leqslant 10\,h^{-1}$ Mpc. At these scales, most galaxy pairs are common members of intermediate mass haloes, and
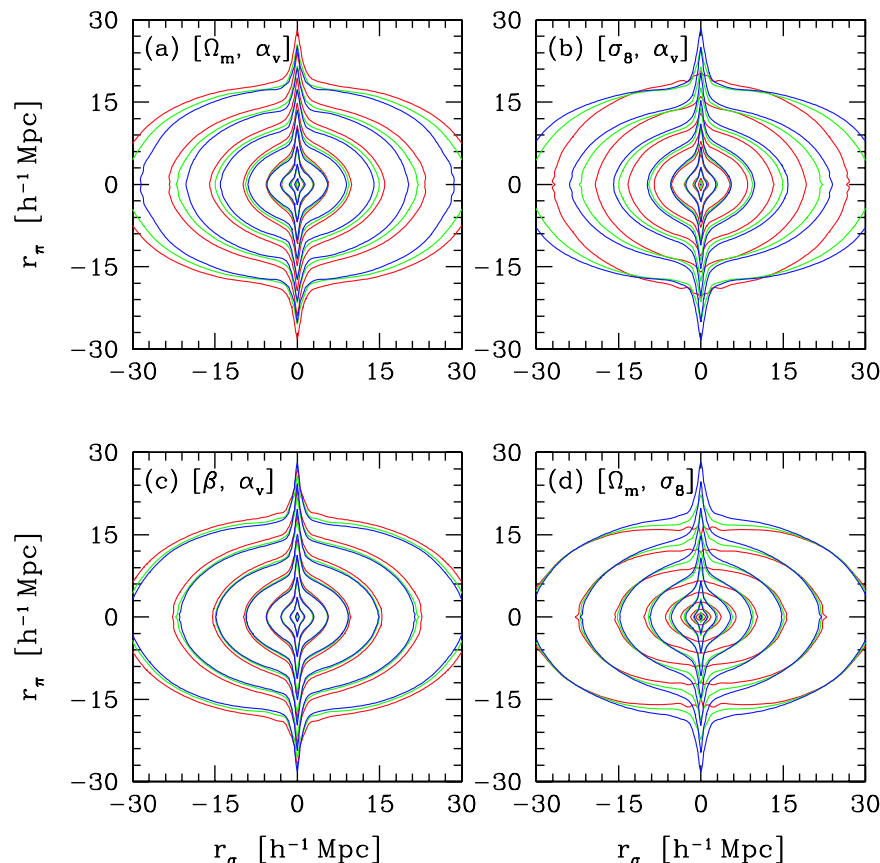
Figure 4. Contour plots of $\xi(r_\sigma, r_\pi)$ in the r_σ–r_π plane, for the four sets of simulations listed in Table 2. The contours are separated by factors of 2 in $\xi(r_\sigma, r_\pi)$, with the outermost contours representing $\xi(r_\sigma, r_\pi) = 2^{-4}$. (a) Models with $\Omega_m = 0.3, \alpha_v = 1$ and $\sigma_8 = 0.95$ (red), $\sigma_8 = 0.80$ (green), $\sigma_8 = 0.60$ (blue). (b) Models with $\sigma_8 = 0.8, \alpha_v = 1$ and $\Omega_m = 0.1$ (red), $\Omega_m = 0.3$ (green), $\Omega_m = 0.5$ (blue). (c) Models with $\beta \equiv \Omega_m^{0.6}/b_g = 0.46, \alpha_v = 1$ and $\sigma_8 = 0.95$ (red), $\sigma_8 = 0.80$ (green), $\sigma_8 = 0.60$ (blue). (d) Models with $\Omega_m = 0.3, \sigma_8 = 0.8$ and $\alpha_v = 0$ (red), $\alpha_v = 0.8$ (green), $\alpha_v = 1.2$ (blue).

the FOG distortion depends on the masses of those haloes. The halo mass function is only weakly dependent on σ_8 at these intermediate masses, so the contours converge. However, a high-σ_8 model has more high-mass haloes with large virial velocity dispersions, so at large r_π the contours extend further for higher σ_8.

Fig. 4(b) shows a model sequence in which $\sigma_8 = 0.8, \alpha_v = 1$, and $\Omega_m = 0.1$ (red), 0.3 (green) and 0.5 (blue). The flattening of contours at large r_σ and elongation at small r_σ both increase with Ω_m, since a higher-density universe has larger amplitude coherent flows and more massive haloes. While the large-scale distortions have a similar qualitative dependence on σ_8 and Ω_m, the FOG distortions show an important difference. Changing Ω_m shifts the halo mass function coherently at all masses, but changing σ_8 shifts the high and low ends of the mass function in opposite directions, with little change at intermediate masses. As a result, the FOG contours converge for the varying σ_8 sequence in panel (a) but not for the varying Ω_m sequence in panel (b).

In panel (c), we again vary σ_8 from 0.6 to 0.8 to 0.95, but for each value of σ_8 we choose the value of Ω_m that keeps the combination $\beta = \Omega_m^{0.6}/b_g$ constant. Note that b_g is approximately proportional to σ_8^{-1}, so this sequence has approximately constant $\sigma_8 \Omega_m^{0.6}$, but not exactly (see Section 4.4 for further discussion). Here, the contours overlap almost perfectly on large and intermediate scales, and they are similar even in the FOG regime. While linear theory does not predict the form of $\xi(r_\sigma, r_\pi)$ accurately even on the largest scale shown (see Fig. 6 below), it correctly predicts that the class of models

with constant β is nearly degenerate with respect to redshift-space distortions. The differences in the FOG regime, though difficult to see in this figure, will none the less prove sufficient to distinguish models with the same β but different σ_8.

In panel (d) we explore the effect of velocity bias. This sequence uses the central values of $\Omega_m = 0.3$ and $\sigma_8 = 0.8$ (and thus has constant β), with α_v equal to 0, 0.8 and 1.2. For clarity, we omit the $\alpha_v = 1$ model from the plot. The $\alpha_v = 0$ model, which would represent measurements from a data set with perfect 'FOG compression', has elliptical contours at all scales, with no trace of the elongation at small r_σ. Since velocity bias is applied only within haloes, these contours show that FOG distortions in $\xi(r_\sigma, r_\pi)$ arise entirely from halo internal velocity dispersions. At larger scales, the $\alpha_v = 0$ model begins to coincide with the others when $r_\sigma \gtrsim r_\pi$. The models with $\alpha_v = 0.8$ and 1.2 diverge at approximately the same location, with higher α_v resulting in a stronger FOG effect. The small-scale dispersion affects any global measure of the shape of $\xi(r_\sigma, r_\pi)$ contours, such as quadrupole-to-monopole ratios, but it has only a small effect at large r_σ *and* r_π. We have also created two models, not shown in this figure, with no satellite velocity bias but with $\alpha_{vc} = 0.2$ and 1. These models will be discussed in subsequent sections.

For the remainder of the paper, we will refer to these four model sequences by writing the parameters that are held constant in square brackets. Panel (a) plots the $[\Omega_m, \alpha_v]$ sequence, panel (b) plots the $[\sigma_8, \alpha_v]$ sequence, panel (c) plots the M_c sequence and panel (d)

Table 2. Properties of the mock galaxy distributions.

$[\Omega_m, \alpha_v]$			$[\sigma_8, \alpha_v]$			$[\beta, \alpha_v]$			$[\Omega_m, \sigma_8]$		
Ω_m	σ_8	β	Ω_m	σ_8	β	Ω_m	σ_8	β	α_v	α_{vc}	β
0.3	0.95	0.53	0.1	0.8	0.24	0.24	0.95	0.46	0.0	0.0	0.46
0.3	0.90	0.51	0.2	0.8	0.36	0.26	0.90	0.46	0.8	0.0	0.46
0.3	0.80	0.46	0.3	0.8	0.46	0.3	0.80	0.46	1.0	0.0	0.46
0.3	0.70	0.41	0.4	0.8	0.55	0.36	0.70	0.46	1.2	0.0	0.46
0.3	0.60	0.36	0.5	0.8	0.63	0.47	0.60	0.46	1.0	0.2	0.46

Note. In the first three sequences, $\alpha_v = 1$ and $\alpha_{vc} = 0$. The HOD parameters and bias factors b_g for each value of σ_8 are listed in Table 1.
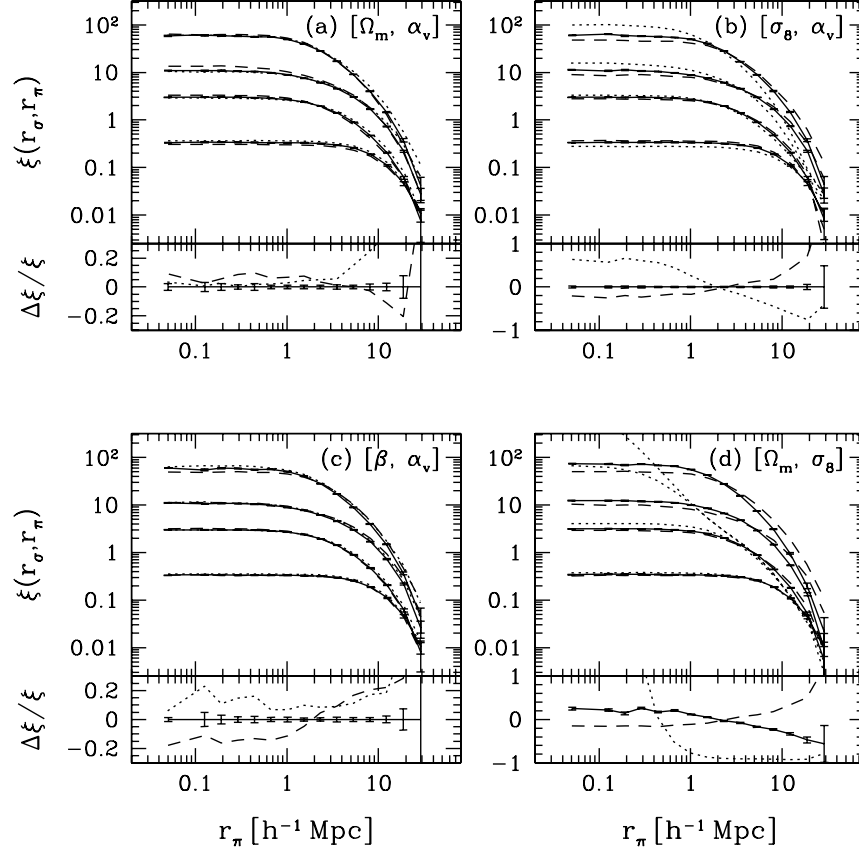

Figure 5. Redshift-space correlation functions for the same models as in Fig. 4, now plotted in the slice format, which allows easier identification of the small-scale distortion. In each panel, curves represent $r_\sigma = 0.12, 0.46, 2.54$ and $14.2\,h^{-1}$ Mpc from top to bottom. At the bottom of each panel, the fractional difference with respect to the central model is shown for the $r_\sigma = 0.12\,h^{-1}$ Mpc curve. (a) Model with $\Omega_m = 0.3, \alpha_v = 1$ and $\sigma_8 = 0.95$ (dotted), $\sigma_8 = 0.80$ (solid), $\sigma_8 = 0.60$ (dashed). (b) Models with $\sigma_8 = 0.8, \alpha_v = 1$ and $\Omega_m = 0.1$ (dotted), $\Omega_m = 0.3$ (solid), $\Omega_m = 0.5$ (dashed). (c) Models with $\beta \equiv \Omega_m^{0.6}/b_g = 0.46, \alpha_v = 1$ and $\sigma_8 = 0.95$ (dotted), $\sigma_8 = 0.80$ (solid), $\sigma_8 = 0.60$ (dashed). (d) Models with $\Omega_m = 0.3, \sigma_8 = 0.8$ and $\alpha_v = 0$ (dotted), $\alpha_v = 0.8$ (solid), $\alpha_v = 1.2$ (dashed). Errors are the run-to-run dispersion divided by $\sqrt{14}$ to calculate the error in the mean. Error bars are only plotted for the solid lines to avoid crowding.

plots the $[\Omega_m, \sigma_8]$ sequence. The values of $\Omega_m, \sigma_8, \beta, \alpha_v$ and α_{vc} for these four model sequences are listed in Table 2.

Fig. 5 plots the same results as Fig. 4, but now in the form of Fig. 3, showing slices at fixed values of r_σ. For each model, the top two curves trace out the FOG distortions at $r_\sigma \approx 0.12\,h^{-1}$ Mpc and $r_\sigma = 0.46\,h^{-1}$ Mpc, allowing discrimination of models in the FOG regime that is difficult from the contour plots alone.

In panel (a), changes in σ_8 at fixed $[\Omega_m, \alpha_v]$ have only a small effect on the FOG distortions at $r_\sigma = 0.12\,h^{-1}$ Mpc, though even these changes are significant relative to our statistical error bars, which are comparable to the line width. At $r_\sigma = 14\,h^{-1}$ Mpc, the

high-σ_8 model has higher $\xi(r_\sigma, r_\pi)$ at all r_π, but the large-scale distortions are more difficult to discriminate in this representation compared to the contour plot (Fig. 4a).

In the remaining panels, parameter changes have a marked effect on the FOG distortions at small r_σ. In particular, the models with constant M_c, which have nearly identical large-scale distortions, show a ~40 per cent change in $\xi(r_\sigma, r_\pi)$ at small (r_σ, r_π) as σ_8 rises from 0.6 to 0.95 (Fig. 5c). While the separation of lines is not dramatic on a plot spanning five decades on the y-axis, differences of tens of per cent should be easily measurable at these scales in the samples the size of the 2dFGRS and SDSS. Changing α_v from
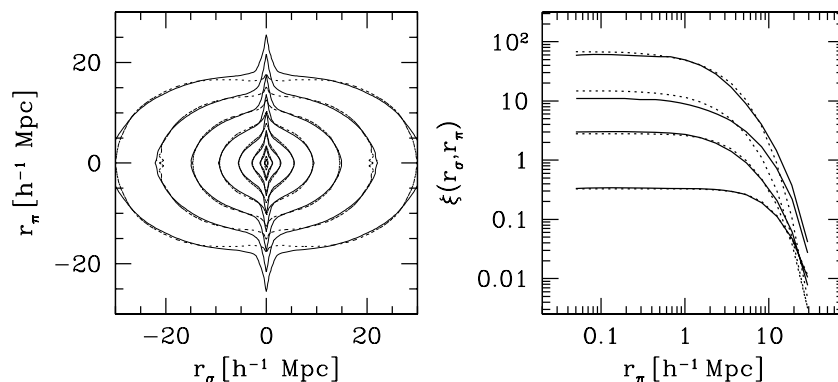
Figure 6. Numerical results for the central model ($\Omega_{\rm m} = 0.3, \sigma_8 = 0.8, \alpha_{\rm v} = 1$) compared to the best-fitting linear–exponential model. The solid lines are the numerical results and the dotted lines are the model. To fit the data, the exact value of β was used, and the best-fitting dispersion $\sigma_8 = 418\,{\rm km\,s^{-1}}$ was found by χ^2 minimization. Contour levels and r_σ values are the same as those used in Figs 4 and 5.
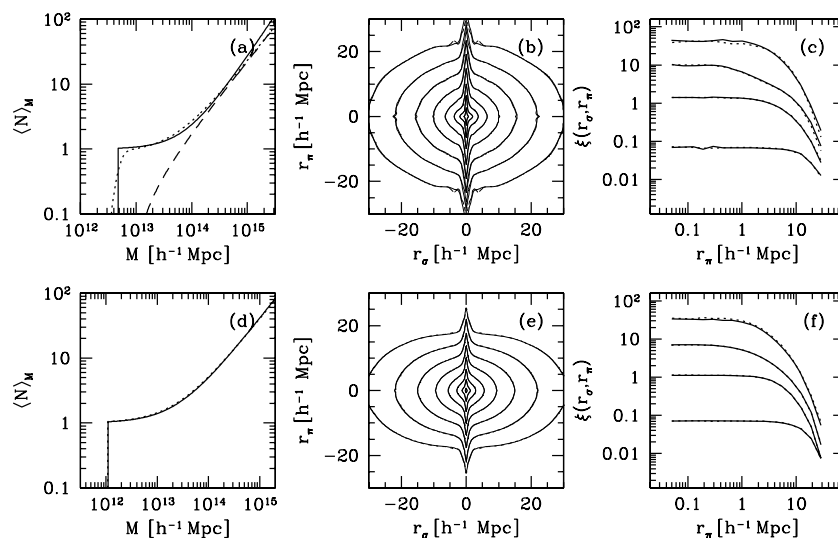
Figure 7. The influence of HOD parametrization or halo concentration on predicted redshift-space distortions, when HOD parameters are chosen to yield the same real-space galaxy correlation function. All models assume $\Omega_{\rm m} = 0.3, \sigma_8 = 0.8, \alpha_{\rm v} = 1$. The top row compares results from our standard three-parameter HOD to the five-parameter HOD of Zheng et al. (2004). (a) Mean occupation functions $\langle N \rangle_M$ for the three-parameter HOD (solid line) and the five-parameter HOD (dotted line). The dashed curve is the satellite contribution to $\langle N \rangle_M$ for the five-parameter HOD. (b) $\xi(r_\sigma, r_\pi)$ contour plots for the three-parameter HOD (solid line) and the five-parameter HOD (dotted line, virtually indistinguishable). (c) Slices in r_σ–r_π for the three-parameter HOD (solid lines) and five-parameter HOD (dotted lines). (d)–(f) Similar to (a)–(c), but dotted curves represent a model in which concentrations have been reduced by factor of 2 and the HOD parameters (in the three-parameter model) have been adjusted to maintain the small-scale correlation function.

0.8 to 1.2 has an effect of similar magnitude, though it differs in detailed form (Fig. 5d).

Fig. 6 compares our numerical results for the central model ($\Omega_{\rm m} = 0.3, \sigma_8 = 0.8, \alpha_{\rm v} = 1$) to the analytic, linear–exponential model of equation (2). We fix β to the true value of 0.46 and vary $\sigma_{\rm v}$ to minimize χ^2 for all data at separations larger than $10\,h^{-1}$ Mpc (we get similar $\sigma_{\rm v}$ if we use data at all separations). The linear–exponential model describes the large-scale distortions fairly well, though even here there are systematic differences between the numerical $\xi(r_\sigma, r_\pi)$ contours and the model fit. The model does a poor job of replicating the FOG distortions at large r_π, a failure that is evident in both the contour plots and the line plots. These deficiencies of the linear–exponential model can also be seen in its application to the 2dFGRS data by Peacock et al. (2001; see their fig. 2). There, the measured distortions at small r_σ clearly extend past the model predictions, even though the FOG effect has been smoothed

relative to our plots here by the larger bin size. We can force the linear–exponential model to better match the FOG distortions by adopting a higher $\sigma_{\rm v}$, but the fit at large scales is then severely degraded.

When analysing observational data, we must infer the galaxy HOD by fitting parametrized models to the measured real-space clustering (e.g. the projected correlation function). We anticipate that redshift-space distortions will be insensitive to the adopted HOD parametrization so long as the model reproduces the observed real-space correlation function. Fig. 7 demonstrates the validity of this conjecture. We first populate the haloes of our $\sigma_8 = 0.8, \Omega_{\rm m} = 0.3\,N$-body simulations using a five-parameter HOD model fit to results of a hydrodynamic simulation (Zheng et al. 2004), in which the galaxy space density is $2.5 \times 10^{-3}\,(h^{-1}\,{\rm Mpc})^{-3}$. This parametrization incorporates adjustable smooth cut-offs in the central and satellite galaxy mean occupation functions, and it can achieve an essentially

perfect fit to the predictions of semi-analytic and numerical models of galaxy formation (Zheng et al. 2004). We then fit parameters of our restricted, three-parameter HOD model to reproduce the correlation function of the five-parameter model as closely as possible, obtaining agreement similar to that in Fig. 2. Fig. 7(a) shows the original and fitted mean occupation functions, and Figs 7(b) and (c) show $\xi(r_\sigma, r_\pi)$ for the two models, in the format of Figs 4 and 5, respectively. While the sharp cut-off model cannot represent the $\langle N \rangle_M$ of the input model exactly, it predicts essentially indistinguishable redshift-space distortions. The large-scale distortions for both models are weaker than those in Figs 4 and 5 because our HOD parameters are matched to a strongly clustered galaxy sample with higher b_g and consequently lower β.

As discussed in Section 2.2, our HOD models assume that satellite galaxies in haloes have the same radial profile as the dark matter. If we change this assumption when fitting the observed correlation function, or if we make this assumption but it does not hold in the real universe, then we will derive slightly different HOD parameters, which in turn will change the redshift-space distortions. We test our sensitivity to the radial profile assumption by creating a model that matches $\xi_R(r)$ of our standard central model but uses satellite profile concentrations lower than those of the dark matter haloes by a factor of 2. Fig. 7(d) shows the mean occupation functions of the two models. The low-concentration model has a lower M_1 to create more close one-halo pairs, and a lower α to prevent overpopulation of massive haloes. Figs 7(e) and (f) show the redshift-space distortions of the two models. The large-scale distortions of the two models are the same, apparent from both the contour plots and the line plots. The low-concentration model has slightly weaker FOG because it has fewer galaxies in massive haloes, but this difference is barely distinguishable in Fig. 7(f), and the difference in the quantitative measures of small-scale distortion measures introduced in Section 5 is within our statistical errors. We conclude that departures from the standard radial profile by $\leqslant 50$ per cent do not alter our results. Still larger changes might have noticeable effect, since the inferred HODs would predict different non-linear velocity fields, but substantial departures from theoretically predicted dark matter profiles can be detected observationally by measuring satellite galaxy profiles in groups and clusters. Also, if multiple galaxy haloes are dynamically relaxed systems, then internal spatial biases would be accompanied by velocity bias. We address this point quantitatively in Section 5.

4 MEASURES OF LARGE-SCALE DISTORTION AND THE VALUE OF β

The blueprint for cosmological parameter estimation begins at large scales. At these scales, anisotropies are governed by the value of $\beta = \Omega_m^{0.6}/b_g$ (see Fig. 4). The effects of velocity bias are limited and, we will show, straightforward to remove. Values of b_g for our five values of σ_8 are listed in Table 1. We define galaxy bias factors by the ratio of the non-linear, real-space galaxy and matter correlation functions in the range $4 \leqslant r \leqslant 12\,h^{-1}$ Mpc, $b_g{}^2 \equiv \xi_g/\xi_m$, a choice that we discuss further in Section 4.4 below. Changing the range to $10 \leqslant r \leqslant 25\,h^{-1}$ Mpc changes the values by $\lesssim 1$ per cent. In characterizing distortions of the power spectrum or correlation function, we follow the track of Kaiser (1987), Hamilton (1992) and Cole et al. (1994), using either the ratio of the angle-averaged redshift-space quantity to the real-space quantity, or the ratio of the quadrupole moment to the monopole in redshift space. The two methods applied to two statistics provide four measures of large-scale distortions, illustrated by Figs 8–11 below.

4.1 The power spectrum

The angular dependence of the redshift-space galaxy power spectrum can be characterized as a sum of Legendre polynomials, denoted here as $L_l(\mu)$,

$$P_Z(k, \mu) = \sum_{l=0}^{\infty} P_l(k) L_l(\mu). \tag{5}$$

This equation can be inverted to determine each individual multipole by

$$P_l(k) = \frac{2l+1}{2} \int_{-1}^{+1} P_Z(k, \mu) L_l(\mu)\, \mathrm{d}\mu. \tag{6}$$

Statistical symmetry of positive and negative peculiar velocities guarantees that odd multipoles vanish on average. In linear perturbation theory, only the $l = 0$, 2 and 4 moments are non-zero. Equations (1) and (6) yield

$$P_0(k) = \left(1 + \frac{2}{3}\beta + \frac{1}{5}\beta^2\right) P_R(k), \tag{7}$$

$$P_2(k) = \left(\frac{4}{3}\beta + \frac{4}{7}\beta^2\right) P_R(k), \tag{8}$$

for the monopole and the quadrupole, where $P_R(k)$ is the real-space power spectrum. In linear theory, the angle-averaged redshift-space power spectrum $P_0(k)$ is amplified over the real-space power spectrum by a constant factor, and the enhancement of fluctuations along the line of sight produces a positive quadrupole $P_2(k)$ with the same shape as $P_R(k)$. The ratio of the monopole to the real-space power spectrum, $P_{0/R}$, and the quadrupole-to-monopole ratio, $P_{2/0}$, are scale-independent functions of β:

$$P_{0/R}(k) \equiv \frac{P_0(k)}{P_R(k)} = 1 + \frac{2}{3}\beta + \frac{1}{5}\beta^2, \tag{9}$$

$$P_{2/0}(k) \equiv \frac{P_2(k)}{P_0(k)} = \frac{\frac{4}{3}\beta + \frac{4}{7}\beta^2}{1 + \frac{2}{3}\beta + \frac{1}{5}\beta^2}. \tag{10}$$

However, non-linear effects, especially the velocity dispersions in collapsed or collapsing structures, suppress $P_0(k)$ at smallest scales and cause the quadrupole to actually reverse sign in the non-linear regime. In practice, the ratios $P_{0/R}$ and $P_{2/0}$ are monotonically decreasing functions of k, and equations (9) and (10) do not provide accurate estimates of β at scales accessible to high-precision measurements. The use of the linear–exponential model (equation 2) in place of pure linear theory (equation 1) can greatly improve the accuracy of β estimates, but it still does not remove biases entirely (Cole et al. 1995; Hatton & Cole 1999).

To calculate the redshift-space galaxy power spectra for our simulations, we use the same technique as Berlind, Narayanan & Weinberg (2001). In the distant observer approximation, we take an axis of the box as the line of sight, wrap particles around the periodic boundary if their peculiar velocities shift them outside the box, and calculate $P_Z(k, \mu)$ by fast Fourier transform. We use a 200^3 density mesh and treat each axis as an independent line of sight. The multipole moments are calculated by fitting the first three even terms in equation (6). We compute the average from 15 measurements (three projections of five simulations) and the errors by dividing the run-to-run dispersions by $\sqrt{14}$. Figs 8 and 9 show the results of this analysis for $P_{0/R}$ and $P_{2/0}$, respectively, as functions of wavelength $\lambda = 2\pi/k$. Horizontal dotted lines represent the values of $P_{0/R}$ and $P_{2/0}$ predicted by linear theory (equations 9 and 10).
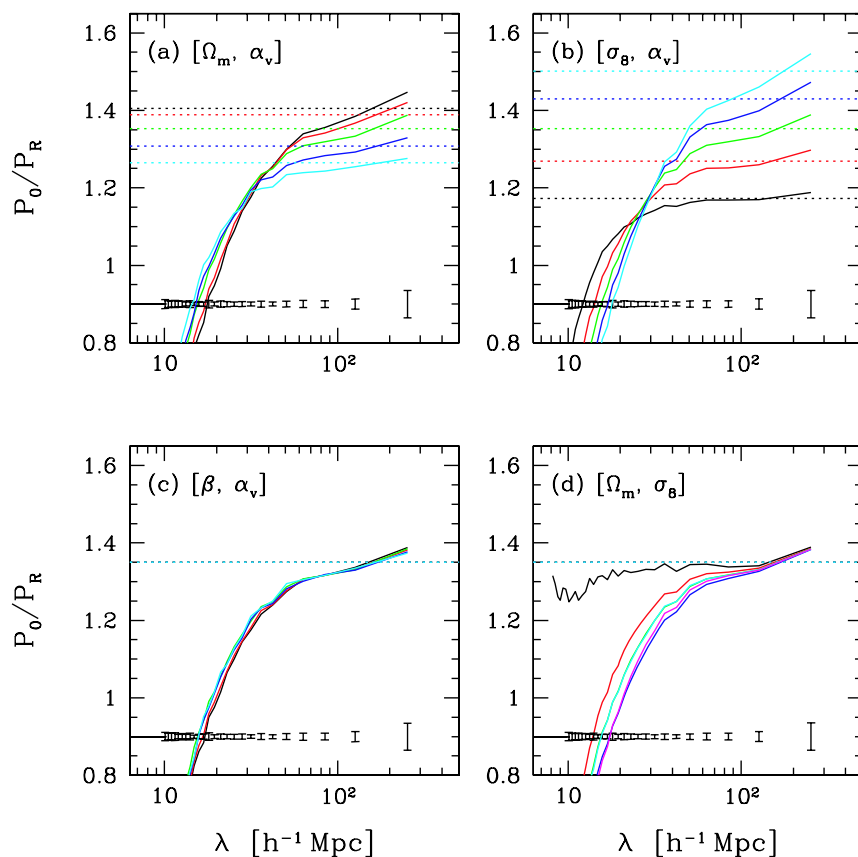
Figure 8. Monopole-to-real-space ratio of the power spectrum, P_0/P_R, as a function of wavelength, up to the fundamental mode of the $253\,h^{-1}$ Mpc box. The dotted lines represent the linear theory prediction for each model for this measure. The error bars plotted at the bottom of each panel are errors in the mean for the central model, which are generally representative of the error bars for the rest of the models in each set. Models run from $\sigma_8 = 0.95$ (black) to $\sigma_8 = 0.6$ (cyan) in panel (a), from $\Omega_m = 0.1$ (black) to $\Omega_m = 0.5$ (cyan) in panel (b) and from $\sigma_8 = 0.95$ (black) to $\sigma_8 = 0.6$ (cyan) in panel (c), with the order of the colours being black, red, green, blue, cyan. In panel (d), models are $\alpha_v = 0$ (black), $\alpha_v = 0.8$ (red), $\alpha_v = 1.0$ (green), $\alpha_v = 1.2$ (blue), $\alpha_{vc} = 0.2$ (cyan, barely separable from green) and $\alpha_{vc} = 1$ (magenta).

Figs 8(a) and (b) plot $P_{0/R}(k)$ for varying σ_8 and Ω_m, respectively. At large λ, $P_{0/R}$ increases with increasing β. But all the curves drop rapidly at scales $\lambda \sim 30\,h^{-1}$ Mpc due to non-linearities. The difficulty in using linear theory to extract β is easily seen; none of the models shows a clear asymptotic value of $P_{0/R}$. An estimate of the linear theory value might be possible for the lowest value of Ω_m or σ_8, but as either parameter increases the slope of the curve at large λ becomes larger. At $\beta \gtrsim 0.4$ the data never converge to the large-scale horizontal asymptote predicted by linear theory, even at the fundamental mode of the box.

For constant M_c, in panel (c), the curves are nearly identical within the error bars, especially at large scales. Thus, even though linear theory does not yield an accurate estimate of β, it predicts the *scaling* of $P_{0/R}$ with cosmological parameters almost perfectly, quantifying the visual impression of Fig. 4(c). In panel (d), the behaviour of the $\alpha_v = 0$ model demonstrates that random dispersion in virialized groups plays a dominant role on suppressing $P_{0/R}$. With the virial motions eliminated, the data for this model remain nearly constant over more than a decade in λ, with the other curves only meeting it at $\lambda \sim 100\,h^{-1}$ Mpc. A sufficiently effective FOG compression technique might therefore allow useful estimation of β from linear theory and $P_{0/R}$.

The other velocity bias models begin to diverge from each other at $\lambda \sim 70\,h^{-1}$ Mpc, again demonstrating that cluster virial velocities affect redshift distortions well into what is normally considered the linear regime. If we allow central galaxies to move with respect to the halo centre-of-mass with bias $\alpha_{vc} = 0.2$, we find barely detectable changes (the line cannot be seen because it is directly beneath the line for the central model). We also plot the model with $\alpha_{vc} = 1$, in which the central galaxy random velocities are the same magnitude as those of dark matter particles. At small scales, adding large central galaxy velocities has roughly the same effect as increasing the *satellite* velocity bias to $\alpha_v = 1.2$, but the $\alpha_{vc} = 1$ model converges with the central model somewhat faster.

Results for the quadrupole-to-monopole ratio are shown in Fig. 9. The model dependence of $P_{2/0}$ is qualitatively similar to that of $P_{0/R}$, though the use of a higher-order multipole leads to substantially larger statistical error. In practice, however, the difference in the errors between $P_{0/R}$ and $P_{2/0}$ would be smaller since $P_R(k)$ is not known a priori and must itself be estimated from the redshift-space power spectrum (see Hamilton, Tegmark & Padmanabhan 2000). As with $P_{0/R}$, the $P_{2/0}$ curves only reach a large-scale asymptote for the lowest values of β. Once again, however, linear theory correctly predicts that models with constant β have the same large-scale distortions. For the fixed $[\Omega_m, \sigma_8]$ model set in panel (d), the $\alpha_v = 0$ model is consistent with linear theory at $\lambda > 20\,h^{-1}$ Mpc. Increasing satellite velocity dispersions suppresses $P_{2/0}$ at steadily larger scales. Central galaxy velocities with $\alpha_{vc} = 0.2$ produce almost no
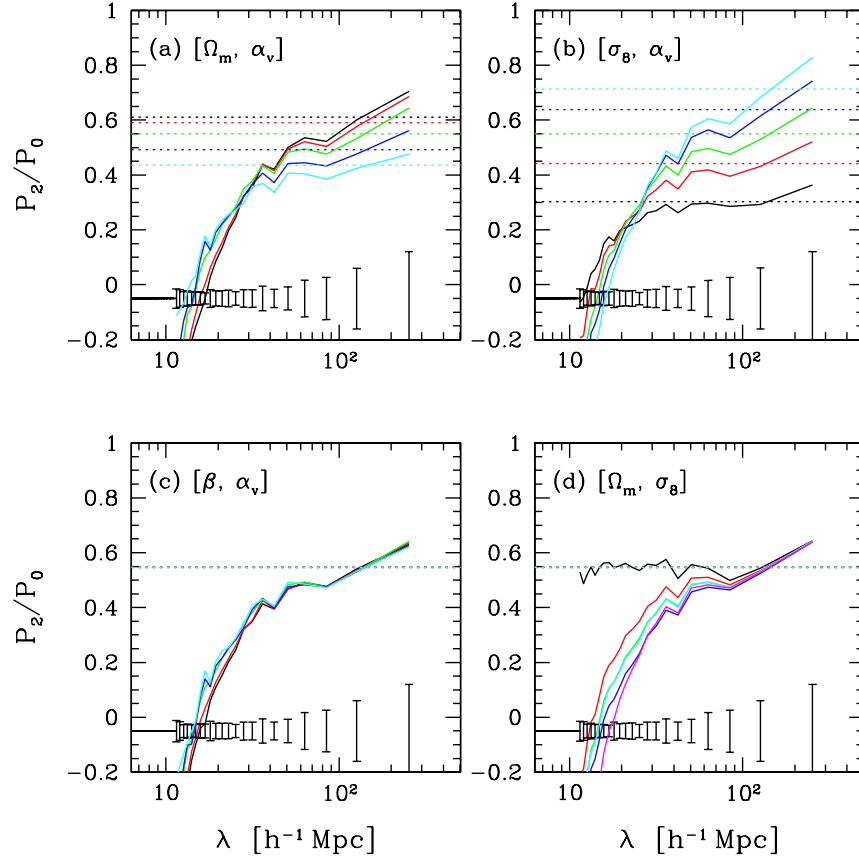
Figure 9. Quadrupole-to-monopole ratio of the redshift-space power spectrum, P_2/P_0, as a function of wavelength, up to the fundamental mode of the $253\,h^{-1}$ Mpc box. The dotted lines and error bars are as in Fig. 8. Models run from $\sigma_8 = 0.95$ (black) to $\sigma_8 = 0.6$ (cyan) in panel (a), from $\Omega_m = 0.1$ (black) to $\Omega_m = 0.5$ (cyan) in panel (b), from $\sigma_8 = 0.95$ (black) to $\sigma_8 = 0.6$ (cyan) in panel (c), with the order of the colours being black, red, green, blue, cyan. In panel (d), models are $\alpha_v = 0$ (black), $\alpha_v = 0.8$ (red), $\alpha_v = 1.0$ (green), $\alpha_v = 1.2$ (blue), $\alpha_{vc} = 0.2$ (cyan, barely separable from green) and $\alpha_{vc} = 1$ (magenta).

change, while the model with $\alpha_{vc} = 1$ shows even stronger suppression than the satellite $\alpha_v = 1.2$ model.

4.2 The correlation function

Since the power spectrum and correlation function are related by Fourier transformation, the linear theory approximation to $P_Z(k, \mu)$ also applies to $\xi(r_\sigma, r_\pi)$. Hamilton (1992) introduced the multipole approximation in configuration space, devising linear theory diagnostics of $\xi(r_\sigma, r_\pi)$ that parallel those in equations (9) and (10). The multipoles of the redshift-space correlation function, $\xi_l(r)$, are calculated by the same inversion formula used in the Fourier domain,

$$\xi_l(r) = \frac{2l + 1}{2} \int_{-1}^{+1} \xi(r_\sigma, r_\pi) L_l(\mu)\, d\mu, \tag{11}$$

where $r = \sqrt{r_\sigma^2 + r_\pi^2}$ and $\mu = r_\pi/r$. The ratio of the monopole, $\xi_0(r)$, to the real-space correlation function, $\xi_R(r)$, exactly parallels equation (9),

$$\xi_{0/R}(r) \equiv \frac{\xi_0(r)}{\xi_R(r)} = 1 + \frac{2}{3}\beta + \frac{1}{5}\beta^2. \tag{12}$$

The quantity

$$Q_\xi(r) \equiv \frac{\xi_2(r)}{\xi_0(r) - \bar{\xi}_0(r)} = \frac{\frac{4}{3}\beta + \frac{4}{7}\beta^2}{1 + \frac{2}{3}\beta + \frac{1}{5}\beta^2} \tag{13}$$

has the same asymptotic value as $P_{2/0}$ in linear theory (assumed for the second equality above). Here $\bar{\xi}_0(r)$ is the volume-averaged

monopole,

$$\bar{\xi}_0(r) = \frac{3}{r^3} \int_0^r \xi_0(s) s^2\, ds. \tag{14}$$

We henceforth refer to Q_ξ as the quadrupole of the redshift-space correlation function. To calculate $\xi_0(r)$ and $\xi_2(r)$, we bin galaxy pairs on a polar grid of logarithmic spacing in r and linear spacing in angle, then perform the integral (11) numerically at each r.

Fig. 10 shows the results for $\xi_{0/R}$, plotted as a linear function of r. In each panel, the curves reach an asymptotic value quickly, near $r = 10\,h^{-1}$ Mpc. In most cases, the asymptote is above the dotted line representing the linear theory prediction. Despite this small systematic bias, which increases with increasing β, this diagnostic does not suffer from non-linear suppression of distortions at large scales; a fit to a constant value is straightforward. Another notable advantage of this diagnostic is that the effects of velocity bias (panel d) are almost negligible beyond $r = 10\,h^{-1}$ Mpc. FOG compression ($\alpha_v = 0$) removes the systematic offset between $\xi_{0/R}$ and the linear theory prediction at $r \sim 10–30\,h^{-1}$ Mpc. This result suggests that the offset is a consequence of FOGs transferring pairs from small separations in real space to large separations in redshift space.

Fig. 11 plots Q_ξ as a linear function of r. These curves resemble those of the power spectrum measures plotted as a function of $\log \lambda$. Models with low values of β reach a horizontal asymptote at large r, while Q_ξ for the high-β models is still increasing at the largest separation. All the curves are under the predicted linear
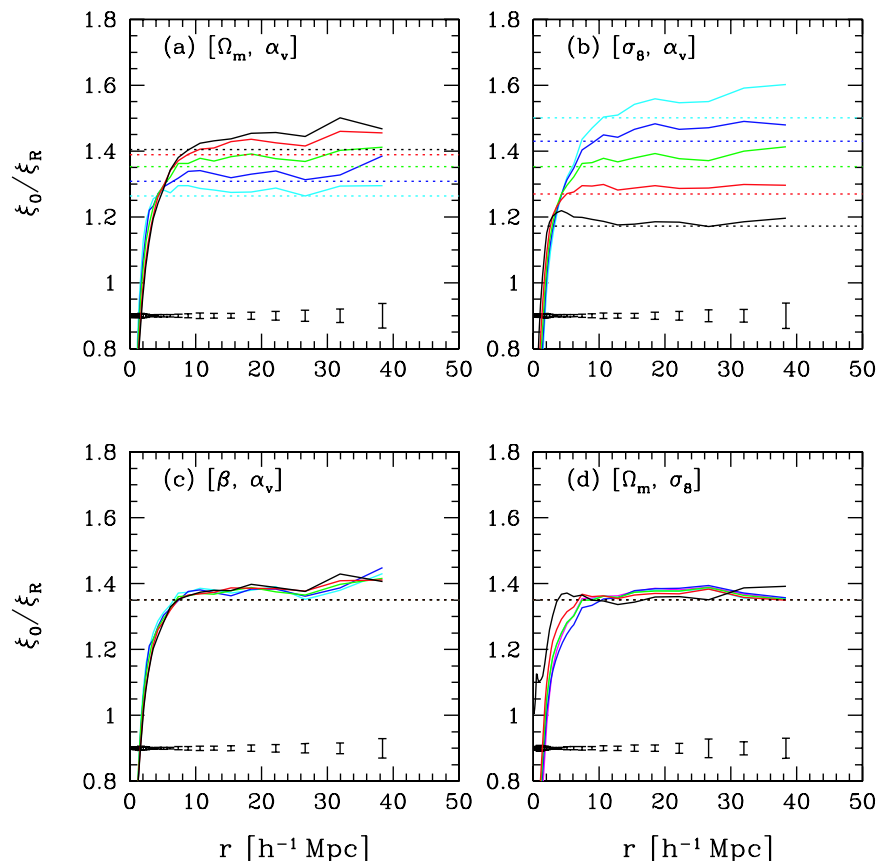
Figure 10. Ratio of the monopole of the redshift-space correlation function to the real-space correlation function, $\xi_{0/R}$, as a function of separation r. The dotted lines and error bars are as in Fig. 8. Models run from $\sigma_8 = 0.95$ (black) to $\sigma_8 = 0.6$ (cyan) in panel (a), from $\Omega_m = 0.1$ (black) to $\Omega_m = 0.5$ (cyan) in panel (b), from $\sigma_8 = 0.95$ (black) to $\sigma_8 = 0.6$ (cyan) in panel (c), with the order of the colours being black, red, green, blue, cyan. In panel (d), models are $\alpha_v = 0$ (black), $\alpha_v = 0.8$ (red), $\alpha_v = 1.0$ (green), $\alpha_v = 1.2$ (blue), $\alpha_{vc} = 0.2$ (cyan, barely separable from green) and $\alpha_{vc} = 1$ (magenta).

theory values, in contrast to the results for $\xi_{0/R}$. Fig. 11(d) shows that small-scale dispersions are the main effect suppressing Q_ξ; with $\alpha_v = 0$, Q_ξ tracks the linear theory prediction down to $r = 10\,h^{-1}$ Mpc. Increasing satellite or central galaxy velocity dispersions drives the non-linear suppression of Q_ξ to larger scales.

The $\xi_{0/R}$ diagnostic reaches its asymptotic value quickly because FOG distortions are strong only at $r \lesssim 2\,h^{-1}$ Mpc, and for r of several h^{-1} Mpc or more these small r_σ separations subtend a small angle in the (r_σ, r_π) plane. In the quadrupole $\xi_2(r)$, the second-order Legendre polynomial $L_2(\mu) = 3(\mu^2 - 1)/2$ gives greater weight to these small-angle structures (see equation 11), with the result that Q_ξ does not approach its linear theory value until $r \approx 30\,h^{-1}$ Mpc. The power spectrum diagnostics $P_{0/R}$ and $P_{2/0}$ show significant deviations from linear theory out to quite large scales, $\lambda \sim 40\,h^{-1}$ Mpc, because the FOG features that are narrow in configurations space become broad in Fourier space.

4.3 Estimating β

The $\alpha_v = 0$ curves in Figs 8(d), 9(d), 10(d) and 11(d) show that β can be estimated fairly accurately using linear theory if FOG distortions are removed by suppressing velocity dispersions in virialized haloes. However, these curves represent a case in which FOG compression is perfect, with haloes identified in real space from the densely sampled dark matter distribution. Any realistic scheme must operate on the sparsely sampled galaxy distribution in redshift

space, and it will suffer from incompleteness and contamination of the halo catalogue and incorrect assignments of galaxies to haloes. The impact of these imperfections on β estimates must be evaluated in the context of a specific group identification scheme applied to a survey with specified depth and geometry, and we will not consider the FOG compression approach further in this paper. Instead, we will use our numerical results to devise fitting procedures that estimate β and a characteristic non-linear scale from measurements of $P_{2/0}(k)$, $P_{0/R}(k)$, $\xi_{0/R}(r)$ and $Q_\xi(r)$. In the remainder of the paper, we use the notation β_{fit} to represent a value of β estimated by one of these fitting procedures, and use β to represent the true model values of $\Omega_m^{0.6}/b_g$. The forms of our fitting functions are arbitrary, motivated by efficacy rather than theoretical arguments, but they all encode the general behaviour of linear distortions at large scales suppressed or reversed by non-linear effects at small scales.

For the quadrupole-to-monopole ratio of the power spectrum, our procedure is similar to that proposed by Hatton & Cole (1999; hereafter HC99), who suggest the fitting formula

$$P_{2/0}(\lambda) = P_{2/0}^{\mathrm{lin}} \left[1 - (\lambda/\lambda_0)^{-1.22} \right]. \qquad (15)$$

Here, $P_{2/0}^{\mathrm{lin}}$ is the linear theory quadrupole distortion, related to β by equation (10), and λ_0 is the non-linear scale at which the quadrupole passes through zero. We make two changes to the HC99 procedure, which, in our experiments, improve the accuracy and robustness of the β estimates. First, we calculate λ_0 by fitting a straight line to the six data points surrounding $P_{2/0} = 0$, instead of leaving it as a fitting
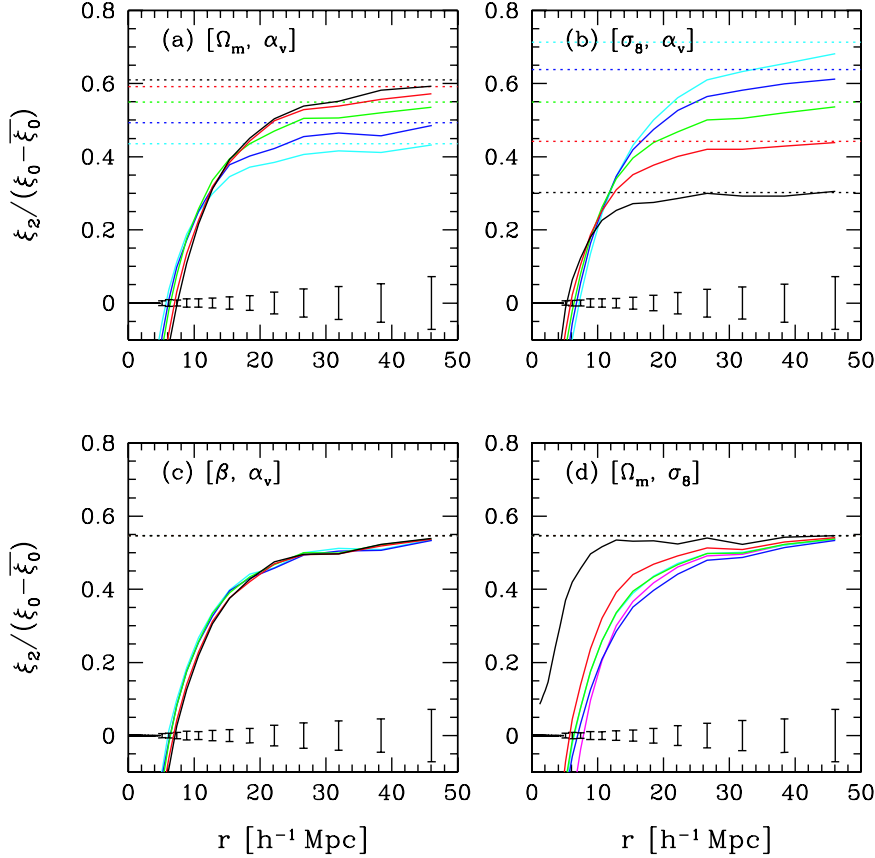
Figure 11. Quadrupole moment of the correlation function, $Q_\xi = \xi_2/(\xi_0 - \bar{\xi}_0)$, as a function of separation. The dotted lines and error bars are as in Fig. 8. Models run from $\sigma_8 = 0.95$ (black) to $\sigma_8 = 0.6$ (cyan) in panel (a), from $\Omega_m = 0.1$ (black) to $\Omega_m = 0.5$ (cyan) in panel (b), from $\sigma_8 = 0.95$ (black) to $\sigma_8 = 0.6$ (cyan) in panel (c), with the order of the colours being black, red, green, blue, cyan. In panel (d), models are $\alpha_v = 0$ (black), $\alpha_v = 0.8$ (red), $\alpha_v = 1.0$ (green), $\alpha_v = 1.2$ (blue), $\alpha_{vc} = 0.2$ (cyan, barely separable from green) and $\alpha_{vc} = 1$ (magenta).

parameter in the global fit. Secondly, we modify equation (15) to

$$P_{2/0}(\lambda) = P_{2/0}^{\text{lin}} \left[1 - \left(\frac{\lambda}{\lambda_0} \right)^{-1.55/(0.45 + P_{2/0}^{\text{lin}})} \right]. \qquad (16)$$

We determine the fitting parameter $P_{2/0}^{\text{lin}}$ by minimizing χ^2 for all data points with $\lambda \geqslant \lambda_0$, ignoring any covariance of errors, and we then solve for β_{fit} using equation (10). Since $P_{2/0}^{\text{lin}}$ varies around ~ 0.55, the exponent in equation (16) is similar to that in the formula of HC99, but including a dependence on $P_{2/0}^{\text{lin}}$ captures the behaviour seen in Fig. 9, where the $P_{2/0}$ curves for higher β models flatten toward their asymptotic values at larger scales.

We use a similar procedure to estimate β from $P_{0/R}(\lambda)$. Here, we define the non-linear scale λ_1 as the wavelength at which $P_Z = P_0$, and we determine it by fitting a straight line to the six data points around $P_{0/R} = 1$. We fit the functional form

$$P_{0/R}(\lambda) = \left(P_{0/R}^{\text{lin}} - 1 \right) \left[1 - \left(\frac{\lambda}{\lambda_1} \right)^{-1.57/(0.50 + \beta_{\text{fit}})} \right] + 1, \qquad (17)$$

where β_{fit} and $P_{0/R}^{\text{lin}}$ are related by equation (9). We estimate β_{fit} by minimizing χ^2 for all data points with $\lambda \geqslant \lambda_1$. As with equation (16), the form of the exponent captures our numerical finding that higher β models approach asymptotic behaviour more slowly. In this case, we found that using β_{fit} rather than $P_{0/R}^{\text{lin}}$ in the denominator of the exponent produced more accurate results.

For Q_ξ, we adopt the fitting function

$$Q_\xi(r) = Q_\xi^{\text{lin}} \left[1 - \left(\frac{1.45}{\beta_{\text{fit}}} \right)^{0.75(1 - r/R_0)} \right], \qquad (18)$$

where once again Q_ξ^{lin} is the free parameter and its relation to β_{fit} is defined in equation (13). The parameter R_0 is the scale at which $\xi_2(r) = 0$. Since the data for Q_ξ are much smoother than those for the power spectrum diagnostics, it is sufficient to fix R_0 by simple interpolation between the two points surrounding $Q_\xi = 0$. We determine β_{fit} by minimizing χ^2 for data points with $r \geqslant R_0$.

For $\xi_{0/R}$, we find that the most effective method to estimate β is simply to fit a straight line to all data above $r = 10 \, h^{-1}$ Mpc, and calculate β_{fit} from linear theory. A minimum scale below $10 \, h^{-1}$ Mpc allows non-linearities to affect the fit, while a larger minimum scale reduces the precision because the error bars increase monotonically with r.

Fig. 12 presents the main quantitative results of this section, showing the fractional error $\epsilon \equiv (\beta_{\text{fit}} - \beta)/\beta$ of the β estimates from $P_{2/0}$, $P_{0/R}$, Q_ξ and $\xi_{0/R}$, using the fitting procedures described above. For the left-hand panels, we fit the curves shown in Figs 8–11, which are averaged over three projections of the five $\Gamma = 0.2$ simulations. Right-hand panels show results of the same procedures for the $\Gamma = 0.12$ simulations.

Squares represent the fixed $[\sigma_8, \alpha_v]$ model sequence, with the Ω_m range 0.1–0.5 producing β values from 0.24 to 0.63 (see Table 2).
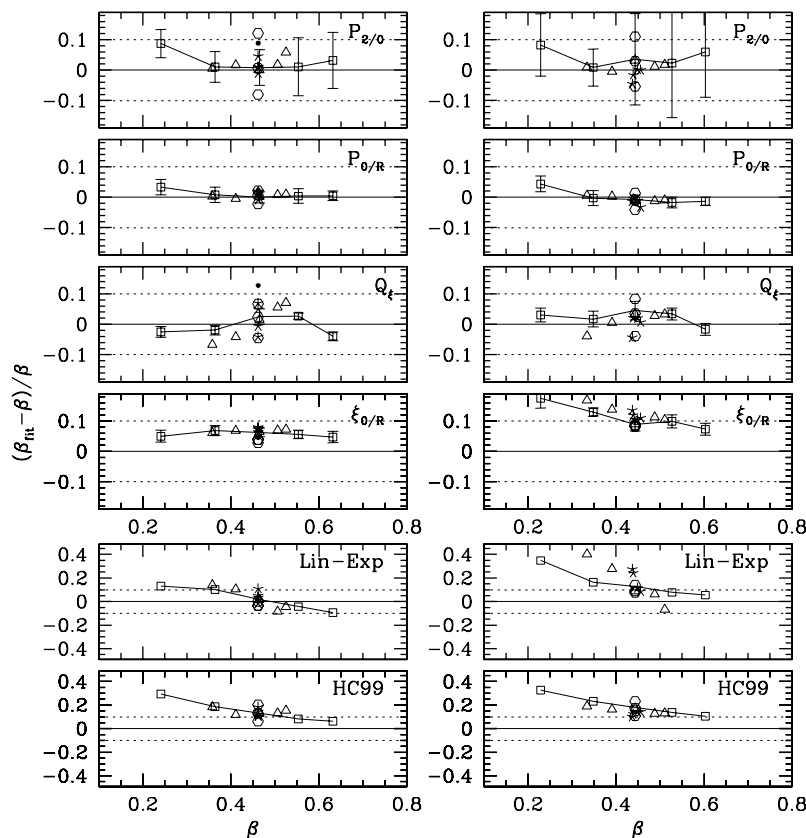
Figure 12. The relative errors in β_{fit} obtained from the fitting functions, for models with $\Gamma = 0.2$ (left-hand panels) and $\Gamma = 0.12$ (right-hand panels). In each panel, the solid lines represent zero error, while the dotted lines are ± 10 per cent error. The four different point types correspond to the four model sets in Table 2: constant $[\Omega_m, \alpha_v]$ (squares), constant $[\sigma_8, \alpha_v]$ (triangles), constant M_c (stars), constant $[\Omega_m, \sigma_8]$ (hexagons). The $\alpha_v = 0$ model is not shown. The $\alpha_{vc} = 1$ model is plotted with a solid circle (left-hand panels only). The bottom panels show, with an expanded vertical scale, the systematic errors of the linear–exponential model and the HC99 fitting method.

The fixed $[\Omega_m, \alpha_v]$ sequence, shown by the triangles, spans a narrower range of $0.36 \leqslant \beta \leqslant 0.53$, since we limit σ_8 to the range 0.6–0.95. Five-point stars represent M_c models, which all have $\beta = 0.46$ by construction. Hexagons represent the $\alpha_v = 0.8$ and $\alpha_v = 1.2$ models from the fixed $[\Omega_m, \sigma_8]$ sequence. The $\alpha_v = 1.0$ model is the same as the central model by definition, and the model with $\alpha_{vc} = 0.2$ is indistinguishable from it in practice, so we omit it from the plot. The $\alpha_{vc} = 1$ model is shown with the small filled circle (left panels only). We do not show results for the FOG compression model because our fitting procedures do not apply to it.

For the fixed $[\sigma_8, \alpha_v]$ sequence, we calculate the statistical uncertainty in our estimate of the fractional error ϵ by separately fitting the five simulations in turn, then dividing the dispersion of the β_{fit} values by $\sqrt{5-1} = 2$ to obtain the uncertainty in the mean. These uncertainties are shown by error bars on the squares in Fig. 12. In many but not all cases, our measurement of the bias in β_{fit} for a given model is consistent with zero, or only marginally inconsistent with it. However, even when the offsets from zero are within the error bars, the trend with model parameters along a sequence may be significant, since all of our models are based on the same set of simulations. The total volume of our simulations is $5 \times (253\, h^{-1}\, \text{Mpc})^3$, equivalent to that of redshift survey covering $8000\, \text{deg}^2$ to a limiting depth of $460\, h^{-1}$ Mpc. Since the three orthogonal projections sample different random orientations of the large-scale structures in each simulation, the effective volume is somewhat larger, though the increase is not a full factor of 3 because real-space structures are

the same in each projection. The error bars in Fig. 12 are therefore similar in magnitude to the statistical error expected from the full SDSS redshift survey, which will cover $8000\, \text{deg}^2$ with a median galaxy redshift ~ 0.1 (Strauss et al. 2002).

Table 3 summarizes the performance of the four β estimators, listing the mean and rms value of the fractional errors plotted in Fig. 12. Note, however, that the numbers depend on the particular set of models we have chosen, so they are only a rough indicator. For $\xi_{0/R}$, our procedure of fitting a straight line to the measurements above $10\, h^{-1}$ Mpc gives a precise but not accurate value of β_{fit}, as seen earlier in Fig. 10. The mean offset is 5.9 per cent for $\Gamma = 0.2$ and 10.9 per cent for $\Gamma = 0.12$. The rms values of ϵ are only slightly larger, consistent with the small scatter around the mean offset seen in Fig. 12, though for $\Gamma = 0.12$ there is a weak but clearly significant trend of ϵ with β. Increasing the minimum fit radius above $10\, h^{-1}$ Mpc reduces the correlation but does not eliminate the higher mean error.

The $P_{0/R}$ fits yield accurate β estimates, with mean errors of less than 1 per cent that are within the statistical uncertainty of our calculations. The rms errors are only 1.3 and 1.8 per cent for $\Gamma = 0.2$ and 0.12, respectively. Velocity bias does have a noticeable effect on the $P_{0/R}$ estimator, with ± 20 per cent changes in α_v producing ∓ 2.4 per cent changes in β_{fit}.

Errors for the quadrupole estimators $P_{2/0}$ and Q_ξ are larger, in part because of our larger statistical uncertainties, but also because of stronger variation with model parameters. Velocity bias has a

Table 3. Errors in $\beta_{\rm fit}$.

Method	$\Gamma = 0.2$		$\Gamma = 0.12$	
	$\langle \epsilon^2 \rangle^{1/2}$ (per cent)	$\langle \epsilon \rangle$ (per cent)	$\langle \epsilon^2 \rangle^{1/2}$ (per cent)	$\langle \epsilon \rangle$ (per cent)
$P_{2/0}$	4.4	1.9	4.2	1.9
$P_{0/R}$	1.3	0.6	1.8	−0.7
Q_ξ	4.3	0.7	3.5	1.7
$\xi_{0/R}$	6.1	5.9	11.3	10.9
Linier plus exponential	9.4	4.2	18.4	14.6
HC99	14.9	14.0	17.3	16.5

significant impact on $P_{2/0}$, with ± 20 per cent changes in $\alpha_{\rm v}$ producing ∓ 9 per cent changes in $\beta_{\rm fit}$ for $\Gamma = 0.2$. For Q_ξ the effect is smaller, ∓ 5.5 per cent. The slope traced by the triangular points shows that the bias of the Q_ξ estimator changes steadily with σ_8, from -6 per cent at $\sigma_8 = 0.6$ to $+8$ per cent at $\sigma_8 = 0.95$ for $\Gamma = 0.2$. A similar trend with σ_8 appears in the constant-β sequence.

For comparison, the lower panels of Fig. 12 show the results of applying the HC99 and linear–exponential models to our simulation results. The HC99 procedure is applied to $P_{2/0}$ measurements with $P_2(k) \geqslant 0$, and we implemented the linear–exponential model by minimizing χ^2 with respect to $\xi(r_\sigma, r_\pi)$ for all data with $r \geqslant 5 \, h^{-1}$ Mpc. Note the larger vertical scale on these panels. The HC99 simulations emphasized values of $\beta \gtrsim 0.6$, and for $\beta \gtrsim 0.5$ we also find it to be fairly accurate, with a bias ~ 10 per cent. However, for lower β values the HC99 procedure substantially overestimates the true β, and our modification defined by equation (16) is a major improvement.

The linear–exponential model performs reasonably well for $\Gamma = 0.2$, but there is a steady trend from positive bias at low β to negative bias at high β, and the rms error of 9.4 per cent is substantially larger than for any of our estimators. Increasing the minimum fitting scale from $5 \, h^{-1}$ Mpc to $10 \, h^{-1}$ Mpc makes little difference. For $\Gamma = 0.12$ the linear–exponential model breaks down more seriously, overestimating β by up to 40 per cent, and showing strong correlation of the $\beta_{\rm fit}$ error with β and with σ_8.

By determining non-linear scales directly from the data, our β-fitting procedures avoid any explicit dependence on σ_8, $\Omega_{\rm m}$ or $\alpha_{\rm v}$. Or course, for known values of σ_8 or $\alpha_{\rm v}$, one could use Fig. 12 to remove the bias of the estimator, further improving its accuracy. Our fitting formulas (16)–(18) are obtained empirically, with only a qualitative relation to a full physical model. However, they successfully describe models with a wide range of physical parameters, and we will show in Section 4.5 below that the non-linear scales in these fits depend on σ_8, $\Omega_{\rm m}$ and $\alpha_{\rm v}$ in physically sensible ways.

The estimates based on redshift-space to real-space ratios, $P_{0/R}$ and $\xi_{0/R}$, perform more robustly than those involving quadrupole moments, once the linear theory estimate from $\xi_{0/R}$ is corrected for systematic bias. Furthermore, the monopole components $P_0(k)$ and $\xi_0(r)$ can be measured with higher precision than the quadrupoles $P_2(k)$ and $\xi_2(r)$, for a data set of fixed size. However, we have not addressed the problem of determining the real-space quantities $P_R(k)$ and $\xi_R(r)$. Hamilton et al. (2000) propose methods for recovering the former, by combining the monopole, quadrupole and hexadecapole on large scales, and using the power in modes transverse to the line of sight on small scales. For $\xi_R(r)$, one can invert the projected correlation function $w_{\rm p}(r_{\rm p})$ (see Davis & Peebles 1983; Zehavi et al. 2005). Alternatively, having fit $w_{\rm p}(r_{\rm p})$ with an HOD model, one can take the three-dimensional correlation function of that model to represent $\xi_R(r)$. It is possible that estimating

$P_R(k)$ or $\xi_R(r)$ in these ways will degrade the performance of the redshift-to-real-space estimators, introducing systematic errors or larger statistical errors. We leave that question to future work that involves mock catalogues tailored to specific data sets.

4.4 From β and $\Omega_{\rm m}$ to σ_8

With sufficiently good observational data, the procedures described in Section 4.3 can provide estimates of $\beta \equiv \Omega_{\rm m}^{0.6}/b_{\rm g}$ that are accurate to a few per cent or better. For a specified value of $\Omega_{\rm m}$, this estimate in turn yields an estimate of $b_{\rm g}$. However, for cosmological purposes we are less interested in $b_{\rm g}$ per se than in the dark matter fluctuation amplitude σ_8. In this paper, we define $b_{\rm g}$ to be the mean value of $[\xi_{\rm g}(r)/\xi_{\rm m}(r)]^{1/2}$ over the range $4 \, h^{-1}$ Mpc $\leqslant r \leqslant 12 \, h^{-1}$ Mpc, where the average is inverse variance weighted and $\xi_{\rm m}(r)$ is the non-linear correlation function of the simulation dark matter particles. The value of $b_{\rm g}$ is insensitive to increases in the inner or outer cut-off on the averaging regions, though it drops if the minimum radius is pushed much below $4 \, h^{-1}$ Mpc. For example, changing the range to $10 \, h^{-1}$ Mpc $\leqslant r \leqslant 25 \, h^{-1}$ Mpc, changes $b_{\rm g}$ of the central model from 1.041 to 1.026, which is the largest change among the five models.

The standard analytic approximation for the large-scale bias factor,

$$b_{\rm g} = \frac{1}{\bar{n}_{\rm g}} \int_0^\infty b_{\rm h}(M) \, \langle N \rangle_M \, \frac{{\rm d}n}{{\rm d}M} \, {\rm d}M, \qquad (19)$$

describes our numerical results for $b_{\rm g}$ with an rms error of 0.4 per cent for $\Gamma = 0.2$ and 0.6 per cent for $\Gamma = 0.12$, if we use the halo bias formula $b_{\rm h}(M)$ of Tinker et al. (2005) and the halo mass function ${\rm d}n/{\rm d}M$ of Jenkins et al. (2001). The bias $b_{\rm g}$ is a monotonically decreasing function of σ_8, since we match the same galaxy correlation function by construction. The most robust way to convert a value of $\beta_{\rm fit}$ to a value of σ_8 (for a specified $\Omega_{\rm m}$) is to consider a sequence of models of increasing σ_8, carry out HOD fits to match the observed projected correlation function $w_{\rm p}(r_{\rm p})$ in each case, compute $b_{\rm g}$ from $\langle N \rangle_M$ using equation (19), and pick the value of σ_8 for which $\Omega_{\rm m}^{0.6}/b_{\rm g} = \beta_{\rm fit}$.

By definition, σ_8 is given by an integral over the linear theory dark matter power spectrum $P_{\rm lin}(k)$. In the linear approximation, where $b_{\rm g}^2 = P_{\rm g}(k)/P_{\rm lin}(k)$, one can use an estimated $b_{\rm g}$ and the measured galaxy power spectrum $P_{\rm g}(k)$ to normalize $P_{\rm lin}(k)$ and thus compute σ_8. Fig. 13 compares our definition of $b_{\rm g}$ (horizontal lines) to the power spectrum ratios $[P_{\rm g}(k)/P_{\rm lin}(k)]^{1/2}$ of the $\Gamma = 0.2$ simulations. For all five values of σ_8, the power spectrum ratios are consistent with a constant asymptotic value at large scales, and this asymptotic value is consistent with the value of $b_{\rm g}$ defined from the correlation function ratio. However, even with our 360^3 simulations, we cannot make this comparison at a precision better than a few per cent because there are relatively few Fourier modes
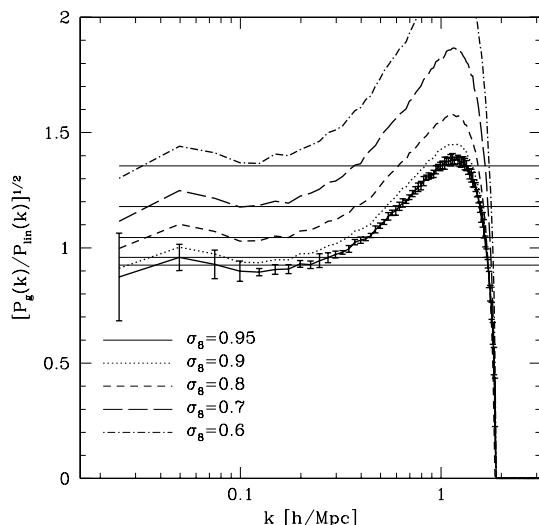
Figure 13. Comparison of bias definitions. Curves show the square root of the ratio of the non-linear galaxy and linear matter power spectra, for the five σ_8 values as indicated. Error bars shown for the $\sigma_8 = 0.95$ model are the error in the mean from five realizations. Thin lines represent the values of b_g measured from the correlation function ratio and used in our definition of β.

in the asymptotic regime. Furthermore, the power spectrum ratios lie slightly above b_g for $\sigma_8 = 0.6$ and slightly below for $\sigma_8 = 0.95$, with a steady trend in between. The same trend appears in Table 1, where the product $\sigma_8 b_g$ rises from 0.81 to 0.88 as σ_8 grows from 0.6 to 0.95. Thus, simply normalizing $P_{\rm lin}(k)$ by $P_g(k)/b_g{}^2$ would not accurately describe our results at the few per cent level. The trend of $\sigma_8 b_g$ arises because we set our HOD parameters by fitting the galaxy correlation function in the linear and non-linear regime; at the few per cent level, our large-scale galaxy correlation function is higher for high σ_8 (see Fig. 2). If we forced a perfect match of the galaxy correlation function at large scales, then $\sigma_8 b_g$ would be constant, but we could no longer match $\xi_R(r)$ as well at small scales, at least with our three-parameter HOD.

The passage from β and Ω_m to σ_8 would be easy if we defined the galaxy bias $b_g = b_8 \equiv \sigma_{8,g}/\sigma_8$, where $\sigma_{8,g}$ is the (non-linear, shot noise subtracted) rms galaxy count fluctuation in $8\,h^{-1}$ Mpc spheres. In this case, one could simply divide $\beta_{\rm fit}$ by $\Omega_m^{0.6}$ and multiply by the measured $\sigma_{8,g}$ to obtain σ_8. We have tried to develop procedures like those in Section 4.3 to estimate $\beta_8 \equiv \Omega_m^{0.6}/b_8$. However, once we tune the estimation formulas to the $\Gamma = 0.2$ simulations, they do not provide accurate results for $\Gamma = 0.12$, in contrast to our procedures for β, which give accurate results for both power spectrum shapes. An $8\,h^{-1}$ Mpc top-hat does not suppress non-linear clustering enough for the bias factor b_8 to approximate bias in the linear regime (as also noted by HC99).

In Paper II, we develop an analytic approach that circumvents the complication of mapping β into the σ_8–$\Omega_m^{0.6}$ parameter space, as the fitting parameters are $(\Omega_m, \sigma_8, \alpha_v)$, without reference to β.

4.5 Length-scales in large-scale distortions

The distortions in redshift-to-real-space and quadrupole-to-monopole ratios in Figs 8 and 11 are driven mainly by galaxy velocity dispersions on small and intermediate scales, which drive down the redshift-space correlation amplitude and reverse the sign of quadrupole distortions. The non-linear length-scales in equa-

tions (9), (10) and (13), and the radius R_1 at which $\xi_0 = \xi_R$, therefore encode information about the parameters Ω_m, σ_8 and α_v, as an increase in any of these variables increases the galaxy velocity dispersion. The dependence of the galaxy velocity dispersion on Ω_m is straightforward: at fixed σ_8, the large-scale velocity field follows the linear theory scaling $\Omega_m^{0.6}$, and the virial velocities of haloes of fixed abundance scale as $\Omega_m^{1/2}$ (ignoring the small dependence of halo concentration on Ω_m). These two effects appear at different scales, but we find that the pairwise galaxy velocity dispersion scales roughly as $\Omega_m^{0.55}$ in our simulations at all separations. For σ_8 and α_v, the situation is more complicated. Velocity bias is most influential at small scales, where the galaxy pairs come from within one halo. At larger scales, a significant fraction of pairs involve the central galaxies of low-mass haloes, and are thus not affected by satellite velocity bias. Inspection of our numerical results suggests that at large separations the pairwise dispersion scales as $\alpha_v^{1/2}$. The power spectrum normalization affects the galaxy velocity dispersion in two ways: at linear scales the halo velocity dispersion increases linearly with σ_8, while the internal velocity dispersions of haloes hosting multiple galaxies increase with σ_8 because of the higher halo masses.

Inspection of the analytic solution for $P_{0/R}$ in the linear–exponential model (see Cole et al. 1995; Section 2.1) implies that the non-linear scale λ_1 where $P_{0/R} = 1$ should scale linearly with the velocity dispersion σ_v at fixed β and approximately as $\beta^{-1/2}$ at fixed σ_v. With the scalings $\sigma_v \propto \Omega_m^{0.55} \alpha_v \sigma_8$ discussed above, we obtain

$$\lambda_1 \propto \beta^{-1/2}\sigma_v \propto \Omega_m^{0.25}\sigma_8^{0.5}\alpha_v, \qquad (20)$$

where the last relation uses $\beta \propto \sigma_8\,\Omega_m^{0.6}$.

The left-hand panel of Fig. 14 plots λ_1 against $\beta\sigma_8^{1/2}\alpha_v^2$, a combination of parameters chosen by trial and error to yield minimal scatter. The numerical data form a tight power law for the $\Gamma = 0.2$ models. The statistical errors derived from the run-to-run
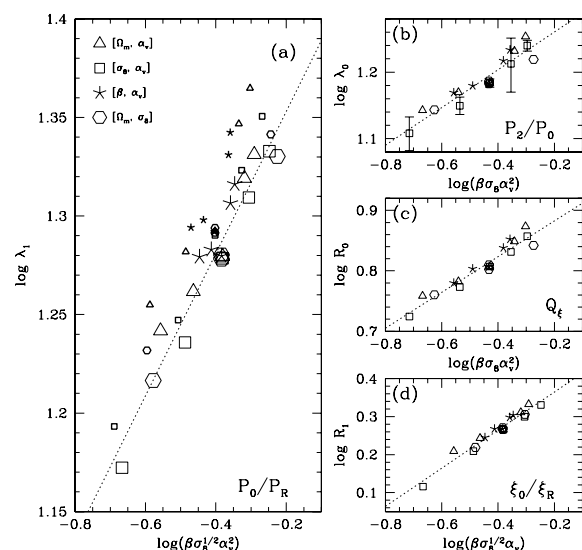

Figure 14. Influence of cosmological parameters on the non-linear length-scales of the large-scale distortion measures. (a) The wavelength λ_1 at which $P_0/P_R = 1$ is plotted against $\beta\sigma_8^{1/2}\alpha_v^2$. Large and small points show the $\Gamma = 0.2$ and 0.12 results, respectively, with point types corresponding to model sequences as indicated in the legend. (b)–(d) Non-linear length-scales for the other three large-scale measures, plotted against the combinations of β, σ_8 and α_v that produce the least scatter, for $\Gamma = 0.2$. Dotted lines show least-squares fits to the data points.

dispersion are of order of the point size, and the fit has a χ^2 per degree of freedom (d.o.f.) of 8.9, indicating that most of the model-to-model scatter is physical in origin. The data for the $\Gamma = 0.12$ models follow the same slope, but the amplitude of the relation is 5 per cent higher, and there is more scatter. The dotted line plotted in the panel is a least-squares fit to the $\Gamma = 0.2$ data. The slope is ~ 0.36, making a scaling of $\lambda_1 = 26.3 \, \Omega_m^{0.22} \sigma_8^{0.54} \alpha_v^{0.72} \, h^{-1}$ Mpc. Given the approximate nature of the arguments behind equation (20), its agreement with this numerically derived scaling is quite good. The lower index on α_v in the numerical results arises because the scale $\lambda_1 \sim 10 \, h^{-1}$ Mpc is outside the one-halo regime where $\sigma_v \propto \alpha_v$ but not fully in the large-scale regime where $\sigma_v \propto \alpha_v^{1/2}$.

In principle, it is possible to use the cosmological dependences of the non-linear scales to constrain parameters by combining the measurements of two or more length-scales. In practice, the significant scatter in the relations limits the usefulness of this approach, as does the apparent dependence of the normalization on power spectrum shape. Instead, in the following section we focus on using the FOG effect to extract information from small-scale distortions.

5 SMALL-SCALE DISTORTION

5.1 Diagnostic power of small-scale distortion

While the non-linear length-scales give some measure of small-scale velocities, we can characterize these velocities more physically and more accurately by focusing on distortions at small r_σ, where they dominate. The traditional measure of small-scale distortions is the pairwise velocity dispersion, but this is not a direct observable; it is extracted from the data by fitting a model that specifies the scale dependence of the mean pairwise velocity of galaxies and the form of the velocity distribution (e.g. Davis & Peebles 1983). We would prefer a quantity that is measured directly from the data, and here we follow the lead of Fisher et al. (1994), who use $\xi(r_\pi)$ at fixed, small r_σ. Referring back to Fig. 5, we see that $\xi(r_\pi)$ at small r_σ is constant for a range of r_π, before turning over at a scale determined by the galaxy velocity dispersion. We can quantify this turnover by the measure $r_{\xi/2}$, the value of r_π at which the correlation function decreases by a factor of 2 relative to its value at $r_\pi = 0$. More generally, one could use the shape of $\xi(r_\pi)/\xi(r_\pi = 0)$ over some range of the line-of-sight separation, scaling by $\xi(r_\pi = 0)$ to remove the sensitivity of the distortion measure to the exact value of the real-space correlation function.

Fig. 15(a) plots $r_{\xi/2}$ against r_σ for the $[\Omega_m, \alpha_v]$ sequence. All the curves have a characteristic wave pattern, which rises to a maximum at $r_\sigma \sim 0.6 \, h^{-1}$ Mpc and reaches a minimum at $r_\sigma \sim 1 \, h^{-1}$ Mpc. The rise at small separation is the result of including one-halo galaxy pairs from increasingly more massive haloes with higher velocity dispersions. The minimum at $1 \, h^{-1}$ Mpc occurs near the one- to two-halo transition in the real-space $\xi_R(r)$. At this separation, two-halo pairs come largely from the central galaxies of lower-mass haloes, so they do not have an internal dispersion contribution, and the halo pairwise velocities themselves are relatively low. At $r_\sigma > 1 \, h^{-1}$ Mpc, all curves monotonically increase, as the internal dispersions of large
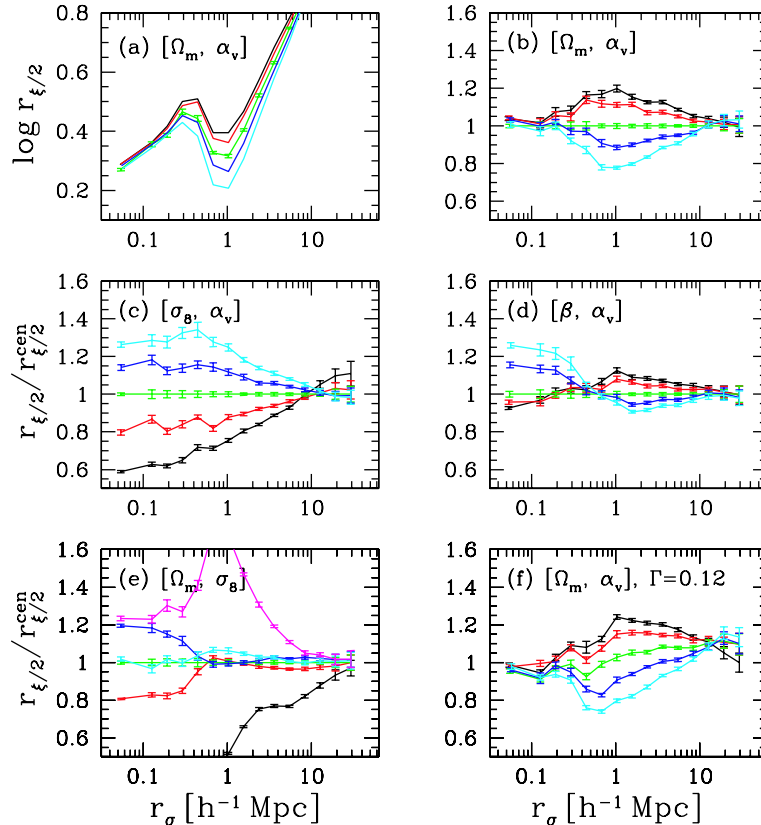

Figure 15. The small-scale distortion parameter, $r_{\xi/2}$, as a function of transverse separation. For panels (b)–(f), each curve has been normalized by the values for the central model, while panel (a) plots the curves as $\log r_{\xi/2}$ for the constant $[\Omega_m, \alpha_v]$ sequence, without normalization. Models run from $\sigma_8 = 0.95$ (black) to $\sigma_8 = 0.6$ (cyan) in panels (a) and (b), from $\Omega_m = 0.1$ (black) to $\Omega_m = 0.5$ (cyan) in panel (c), from $\sigma_8 = 0.95$ (black) to $\sigma_8 = 0.6$ (cyan) in panel (d), with the order of the colours being black, red, green, blue, cyan. In panel (e), models are $\alpha_v = 0$ (black), $\alpha_v = 0.8$ (red), $\alpha_v = 1.0$ (green), $\alpha_v = 1.2$ (blue), $\alpha_{vc} = 0.2$ (cyan) and $\alpha_{vc} = 1$ (magenta). (f) Models are the same as panel (b), but with $\Gamma = 0.12$.
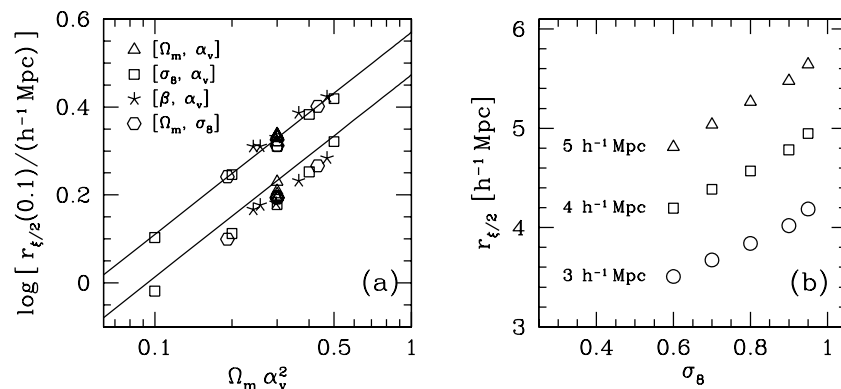
Figure 16. Diagnostic power of the small-scale distortion measure. (a) Points show $r_{\xi/2}(0.1)$ against $\Omega_m \alpha_v{}^2$ for all of the $\Gamma = 0.2$ models, except $\alpha_v = 0$ and $\alpha_{vc} = 1$. The upper line shows a least-squares fit, $r_{\xi/2}(0.1) = 3.7(\Omega_m \alpha_v{}^2)^{0.46}$, with $\chi^2_{d.o.f.} = 1.9$. The lower points, shifted down by 0.2 dex for visual clarity, show the $\Gamma = 0.12$ results. These data lie ~ 7 per cent below the (shifted) line. (b) Dependence of $r_{\xi/2}$ on σ_8 for models in which both the large-scale distortions ($\beta = 0.46$) and the small-scale distortions [$r_{\xi/2}(0.1) = 2.0\,h^{-1}$ Mpc] are fixed to the same values. Circles, squares and triangles represent $r_\sigma = 3, 4$ and $5\,h^{-1}$ Mpc, respectively.

haloes again start to contribute and the pairwise dispersion of haloes themselves increases. To highlight the differences between the models, panels (b)–(f) plot five model sequences where all the curves have been normalized by the values for the central model ($\Omega_m = 0.3$, $\sigma_8 = 0.8$, $\alpha_v = 1$, $\alpha_{vc} = 0$). Panels (b)–(e) show the standard suite from Table 2 and earlier figures. In panel (b), with fixed Ω_m and α_v, changing σ_8 has little effect on $r_{\xi/2}$ at $r_\sigma \leqslant 0.2\,h^{-1}$ Mpc. This separation is small enough that rare, high-mass haloes do not contribute a large fraction of the one-halo galaxy pairs relative to the pairs contributed by haloes with mass $M_h \approx M_1$, where σ_8 has little effect on the halo mass function. The value of σ_8 has a large impact on $r_{\xi/2}$ at $r_\sigma \sim 1\,h^{-1}$ Mpc, the location of the one- to two-halo transition. More high-mass haloes create more large-separation one-halo pairs, extending the one-halo $\xi_R(r)$ to larger r. These pairs have large velocity dispersion and are therefore spread out along the line of sight, increasing $r_{\xi/2}$.

In panel (c), with fixed σ_8 and α_v, changing Ω_m affects $r_{\xi/2}$ at all $r_\sigma \lesssim 10\,h^{-1}$ Mpc. Higher Ω_m increases both halo pairwise velocities and internal velocity dispersions, thus increasing $r_{\xi/2}$ on all scales where dispersion dominates over coherent flows. Panel (d) shows models with constant β and α_v, and thus constant large-scale anisotropy. As expected from the previous results, higher Ω_m models have larger $r_{\xi/2}$ at $r_\sigma \sim 0.1\,h^{-1}$ Mpc, where σ_8 has little impact. At $r_\sigma \sim 1\,h^{-1}$ Mpc, the higher Ω_m models (with lower σ_8) have smaller $r_{\xi/2}$; the depression seen in panel (b) wins out over the enhancement in panel (c). Thus, at fixed β and α_v, the small-scale distortions can break the degeneracy between Ω_m and σ_8.

Panel (e) shows models with varying α_v but constant Ω_m and σ_8 (and thus constant β). Not surprisingly, the $\alpha_v = 0$ model has very small values of $r_{\xi/2}$ relative to the central model at scales less than $10\,h^{-1}$ Mpc. The effect of moderate velocity bias is most significant at the smallest r_σ, with 20 per cent changes in $r_{\xi/2}$ at $r_\sigma = 0.1\,h^{-1}$ Mpc for $\alpha_v = 1.2$ or 0.8. However, these α_v variations have little impact at large r_σ, where 20 per cent changes of internal velocity dispersions are small compared to halo velocities themselves, and the effect is essentially zero at $r_\sigma \sim 1\,h^{-1}$ Mpc. At this separation, two-halo pairs begin to dominate $\xi(r_\sigma, r_\pi)$, but r_σ is still smaller than the virial radii of large haloes. Most pairs therefore come from haloes that contain a central galaxy and no satellites, and the value of α_v has no effect. Central galaxy velocities have

maximum effect at the $\sim 1\,h^{-1}$ Mpc scale, for the same reason. Setting $\alpha_{vc} = 0.2$ boosts $r_{\xi/2}$ by 5–10 per cent at this r_σ, while treating central galaxies like satellites ($\alpha_{vc} = 1$) boosts it by a factor of 2.

Panel (f) plots the results for the constant $[\Omega_m, \alpha_v]$ sequence with $\Gamma = 0.12$, once again normalized by the $\Gamma = 0.2$ central model. As in panel (b), σ_8 has minimal effect at small scales and makes the most difference at $r_\sigma \sim 1 - 2\,h^{-1}$ Mpc. The higher $r_{\xi/2}$ at large r_σ in the $\Gamma = 0.12$ models probably reflects the shallower real-space correlation function at these scales.

Fig. 15 demonstrates that $r_{\xi/2}$ is a robust diagnostic for Ω_m and α_v when r_σ is small, independent of σ_8 or Γ. In Fig. 16(a), the upper points plot $r_{\xi/2}(0.1)$ against $\Omega_m \alpha_v{}^2$ for all of the $\Gamma = 0.2$ models (except those with $\alpha_v = 0$ and $\alpha_{vc} = 1$). The data follow a power law with a slope of 0.46 and minimal scatter. For one-halo pairs, the redshift-space separation depends on relative velocities, which are proportional to $\Omega_m{}^{1/2} \alpha_v$, and one might therefore expect a slope of 0.5. Because there is a small two-halo contribution to $\xi(r_\sigma, r_\pi)$ at these separations, the slope deviates slightly from this expectation. The data for $\Gamma = 0.12$ follow a similar power law, but with a normalization ~ 7 per cent lower, as expected from the results in Fig. 15(f). This offset may arise partly from the difference in the real-space correlation function, which is shallower for $\Gamma = 0.12$, and partly from the difference in the halo mass function, which changes the relative importance of pairs from different haloes.

The values of β and $r_{\xi/2}(0.1)$ provide two observable constraints in our three-dimensional (Ω_m, σ_8, α_v) parameter space, measuring the combinations $\sigma_8 \Omega_m^{0.6}$ and $\Omega_m \alpha_v{}^2$. A measurement of $r_{\xi/2}$ at somewhat larger r_σ has the possibility of providing a third constraint on a different combination of these parameters. Based on the power-law fit in Fig. 16(a), each constant-β model was given the value of α_v required to match $r_{\xi/2}(0.1)$ of the central model. Relative to Fig. 15(d) at fixed M_c, this scaling brings curves together at $r_\sigma < 1\,h^{-1}$ Mpc, but it makes little difference at larger separations where α_v has little effect. Differentiating between adjacent models requires high precision in the measurements, but there is a clear, 20 per cent separation between the low and high values of σ_8 with this diagnostic. In Fig. 16(b), we plot $r_{\xi/2}$ against σ_8 for $r_\sigma = 3, 4$ and $5\,h^{-1}$ Mpc. At each transverse separation, there is a monotonic, nearly linear trend with σ_8 once β and $r_{\xi/2}(0.1)$
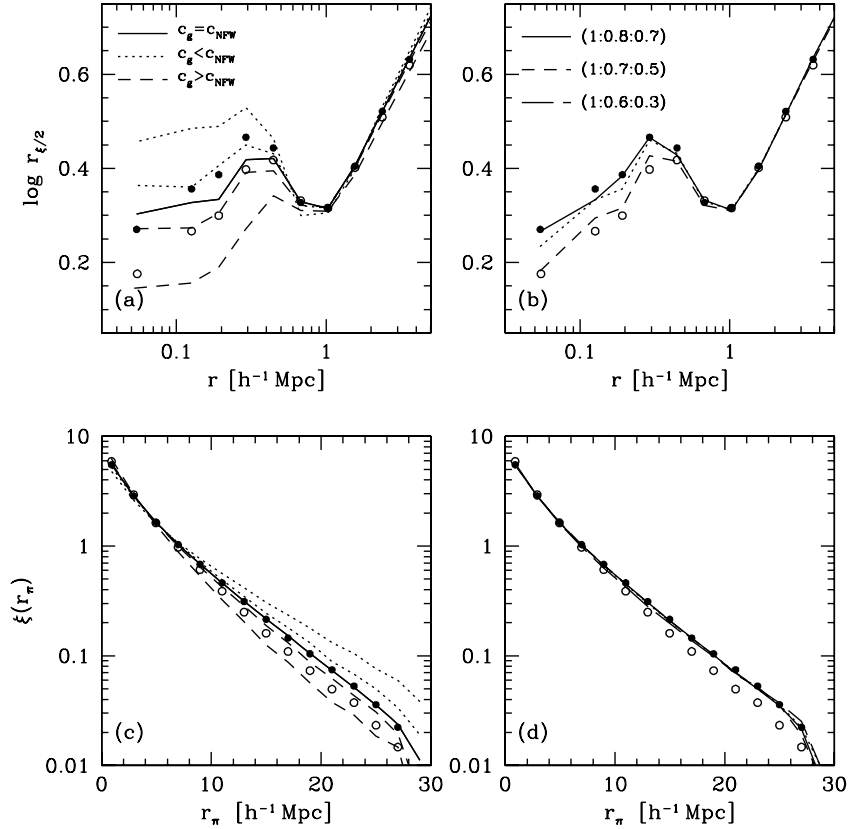
Figure 17. The effect of non-isothermality and velocity anisotropy on the FOG effect. Panel (a): The lines plot $r_{\xi/2}$ for the fiducial cosmology, but satellite velocities are drawn from a dispersion profile determined from the Jeans equation at each halo mass. The solid line is where the galaxies have the same density profile as the dark matter. The dashed lines represent models in which the galaxies are more centrally concentrated than the dark matter: $c_g/c_m = 1.2$ (upper dashed line) and $c_g/c_m = 2$ (lower dashed line). The dotted lines are models in which the galaxies are less centrally concentrated than the dark matter: $c_g/c_m = 0.8$ (upper dotted line) and $c_g/c_m = 0.5$ (lower dotted line). For comparison, the solid circles are the data for the central model and the open circles are for the model with $\alpha_v = 0.8$. Panel (b): Models with velocity anisotropy along the principal axes of each halo. The numbers in the key denote the ratios of the velocity dispersion in each direction. Panel (c): The same models as (a), but $\xi(r_\pi)$ is plotted against the line-of-sight direction r_π. Panel (d): The same models as (b), but $\xi(r_\pi)$ is plotted against line-of-sight direction r_π. For models with non-isothermal satellite dispersions, the effect can be quantified with the velocity bias parameter α_v. For anisotropic models, the effect is different for the two statistics shown in panels (b) and (d), but an unreasonably large anisotropy is required.

have been fixed. These results allow for unambiguous determination of σ_8, breaking the third and last degeneracy in the parameter space.

Fig. 16(b) assumes $\alpha_{vc} = 0$, and central galaxy velocities could interfere with this approach to breaking degeneracies. For example, adopting $\alpha_{vc} = 0.2$ increases $r_{\xi/2}(0.1)$ by ~5 per cent, which is of order of the effect of changing σ_8 by 0.1. However, the effects of moderate α_{vc} on this measure go away at scales larger than $3 h^{-1}$ Mpc, where there is still clear model differentiation in Figs 15(d) and 16(b). As we have already noted, physical arguments and hydrodynamic simulations support the assumption of low α_{vc}, but further theoretical and observational investigation of this point is warranted.

5.2 Departures from isothermality and orbital isotropy

Throughout this paper, we have assumed isotropy and isothermality in the velocity distribution of satellite galaxies. In Fig. 17 we demonstrate that the influence of these two effects is encompassed by a simple velocity bias parameter.

Because the NFW profile deviates from a logarithmic slope of -2 at large and small radii, the velocity dispersion of dark matter particles will depend on radius. Assuming a spherical, relaxed system,

the velocity dispersion profile can be obtained by solving spherical Jeans equation, i.e.

$$\sigma^2(r) = \frac{1}{n_{sat}(r)} \int_r^\infty n_{sat}(x) \frac{G M(x)}{x^2} \, dx, \tag{21}$$

where $n_{sat}(r)$ is the number density of satellite galaxies at radius r, and $M(r)$ is the halo mass contained within r (e.g. van den Bosch et al. 2004). At radii smaller than the NFW scale radius r_s, $\sigma(r)$ increases monotonically with r, and falls at $r > r_s$. The mean satellite dispersion for a halo of mass M is therefore

$$\langle \sigma_{sat} \rangle = \frac{4\pi}{\langle N_{sat} \rangle_M} \int_0^{R_{200}} \sigma(r) \, n_{sat}(r) \, r^2 \, dr. \tag{22}$$

At $M \approx 10^{13} \, h^{-1} \, M_\odot$, $\sigma_{200}/\langle \sigma_{sat} \rangle \approx 1$, and at $10^{15} \, h^{-1} \, M_\odot$, this ratio is 1.08.

Fig. 17(a) plots $r_{\xi/2}$ against r_σ for a variety of models with non-isothermal velocity dispersion profiles. For reference, the filled and open circles show the isothermal results from Fig. 15(e) with $\alpha_v = 1$ and 0.8, respectively. The solid line shows $r_{\xi/2}$ for a model in which the galaxies follow the $\sigma(r)$ profile for the dark matter in each halo. To properly compare these calculations to the isothermal results, equation (21) has been normalized such that $\sigma_{200}/\langle \sigma_{sat} \rangle = 1$ at all masses. Even though the mean galaxy dispersion is the

same as the isotropic, $\alpha_{\rm v} = 1$ model, the $r_{\xi/2}$ curve is lower at all $r_\sigma > 0.1\,h^{-1}$ Mpc. The innermost r_σ bin isolates one-halo pairs from the inner regions of haloes where $\sigma(r) > \langle\sigma_{\rm sat}\rangle$. At $r_\sigma > 0.1\,h^{-1}$ Mpc, the majority of one-halo pairs come from the outer regions of haloes, where the local dispersion is below the halo average. At these separations, the difference between the isotropic and NFW dispersion profiles is well-modelled by model with $\alpha_{\rm v} = 0.9$. The innermost bin, $r_\sigma < 0.1\,h^{-1}$ Mpc, is of little importance in the context of SDSS measurements, as fibre collisions preclude the use of this bin.

If the number density profile of satellite galaxies differs from that of the dark matter, equation (21) implies that the mean dispersion of the satellites will differ from σ_{200}. We define the parameter $a_{\rm c} \equiv c_{\rm g}/c_{\rm m}$ as the ratio of the NFW concentration parameter for the galaxies to that of the dark matter. If $a_{\rm c} < 1$, galaxies are less centrally concentrated and will have a higher mean dispersion than the dark matter. If $a_{\rm c} > 1$ the galaxy dispersion will be lower. The dotted lines in panel (a) plot $r_{\xi/2}$ for $a_{\rm c} = 0.5$ (upper line) and $a_{\rm c} = 0.8$ (lower). The dashed lines represent models with $a_{\rm c} = 1.2$ (upper) and $a_{\rm c} = 2.0$ (lower). The mild changes in galaxy concentrations, $a_{\rm c} = 0.8$ and 1.2, are quantitatively similar to the isotropic results with $\alpha_{\rm v} = 1.0$ and 0.8, respectively. The large changes in galaxy concentrations produce substantial changes in the FOGs, similar to $\alpha_{\rm v} = 1.5$ and 0.5.

In panel (b) in Fig. 17, we explore the effect of velocity anisotropy on $r_{\xi/2}$. Dark matter haloes are triaxial objects and, just as the axis ratios of the spatial distribution of particles will be unequal, so too will the axis ratios of the phase-space distribution. The dark matter haloes in our simulations have a mean anisotropy of $\sigma_i : \sigma_j : \sigma_k = 1 : 0.8 : 0.7$, where i, j, k are orthogonal Cartesian directions aligned with the spatial axis ratios of each halo, with a halo-to-halo dispersion in the anisotropy of 0.3 in $\log(1 - \sigma_{j,k}/\sigma_i)$. To model this type of velocity anisotropy in our mock galaxy distributions, each halo is given an anisotropy with a random orientation with respect to the axes of the simulation volume. The rms velocity in each halo is the same as the isotropic case. In panel (b), we plot the results for anisotropies of $(1 : 0.8 : 0.7)$, $(1 : 0.7 : 0.5)$ and $(1 : 0.6 : 0.3)$, all with a dispersion of 0.3 as defined above. The results for $\alpha_{\rm v} = 1.0$ and 0.8 are once again shown for comparison. For the mildest anisotropy there is little difference from the isotropic case. As the anisotropy increases, $r_{\xi/2}$ at small r_σ reduces. For the largest anisotropy, the results are close to a velocity bias of 0.8. The effect of this type of anisotropy is to change the velocity distribution from Gaussian to a distribution close to exponential, with a sharp peak and broad wings. The broad tails to the new distribution do not affect $r_{\xi/2}$ since this measure isolates the FOG effect at $r_\pi \lesssim 3\,h^{-1}$ Mpc. Therefore, the line-of-sight separation of the pairs that affect $r_{\xi/2}$ are reduced, and $r_{\xi/2}$ itself is reduced. However, this effect is only achieved for an unphysically high anisotropy.

Velocity anisotropy is more commonly quantified in the radial and tangential directions, defined as $\beta_{\rm orb} = 1 - \sigma_r/2\sigma_t$. For $-0.4 \leqslant \beta_{\rm orb} \leqslant +0.4$, the results are consistent with no velocity bias. As $\beta_{\rm orb}$ approaches zero, a fully radial distribution, $r_{\xi/2}$ is reduced significantly because radial velocities (in the one-halo term) become orthogonal to the line of sight as r_σ increases to the edge of a halo.

Figs 17(c) and (d) plot the redshift-space correlation function along the line of sight in linearly spaced bins $2\,h^{-1}$ Mpc in length and $[0, 2]\,h^{-1}$ Mpc wide in r_σ. A bin of this width encompasses nearly the entire one-halo term. For this binning, $\xi(r_\pi)$ is nearly exponential, and is dominated by one-halo pairs at $r_\pi > 5\,h^{-1}$ Mpc. In panels (c) and (d), the lines and symbols correspond to the same models

as in panels (a) and (b), respectively. In panel (c), the solid curve representing $a_{\rm c} = 1$ is now equivalent to the $\alpha_{\rm v} = 1$ model. In this wide bin, satellite galaxies are no longer preferentially selected from the inner or outer parts of the halo. All one-halo pairs are selected, therefore differences in $\xi(r_\pi)$ can only originate from differences in $\langle\sigma_{\rm sat}\rangle$. As expected from panel (a), models with $a_{\rm c} < 1$ have higher $\xi(r_\pi)$ than $\alpha_{\rm v} = 1$ and models with $a_{\rm c} > 1$ have lower $\xi(r_\pi)$. The value of $\alpha_{\rm v}$ which is equivalent to the effect created by $a_{\rm c} \neq 1$ can be calculated directly from equation (22).

In panel (d), all models are equivalent to $\alpha_{\rm v} = 1$. At large values of r_π, the differences in the shape of the pairwise velocity distribution for each halo average out, and the relevant quantity is the rms velocity, which is the same in all models.

The velocity bias created by the spatial bias of satellite galaxies in panels (a) and (c) relies on the assumption that both the dark matter haloes and the satellite distribution form a system in equilibrium. High-resolution numerical simulations of dark matter subhaloes (Klypin et al. 1999; Ghigna et al. 2000; Diemand et al. 2004) show that the radial distribution of subhaloes is significantly less concentrated than the dark matter. The same effect is seen in hydrodynamic simulations (Springel et al. 2001; Berlind et al. 2003; Yoshikawa, Jing & Börner 2003; Nagai & Kravtsov 2005). The velocity dispersion of the satellite galaxies is roughly equal to that of the dark matter, not the large bias implied by equation (21). The velocity bias inferred from the collisionless results is generally somewhat larger than unity, while in the hydrodynamic simulations the velocity bias is slightly less than unity, even though the distribution of satellite galaxies in less concentrated than the dark matter. Satellite galaxies may not form a relaxed system, and therefore not subject to the Jeans equation, because they have been recently accreted or due to dynamical friction, which would slow galaxies. Dynamical friction would be more effective in hydrodynamic simulations because subhaloes with stars and baryons within them are more centrally concentrated and less likely to be tidally disrupted. For modelling the non-linear redshift distortions, the best approach is to leave spatial and velocity biases as separate free parameters and fit for both from the real- and redshift-space clustering data.

6 DISCUSSION

Our results provide a blueprint for obtaining constraints in the $(\Omega_{\rm m}, \sigma_8, \alpha_{\rm v})$ parameter space from measurements of clustering anisotropy in redshift space. For each model in the parameter space, one first chooses HOD parameters to reproduce measurements of the projected galaxy correlation function $w_{\rm p}(r_{\rm p})$, which depends only on the real-space correlation function $\xi_R(r)$. If the assumed power spectrum shape is correct, it will generally be possible to match $w_{\rm p}(r_{\rm p})$ well for a wide range of σ_8 and $\Omega_{\rm m}$. At large scales, the anisotropy ratios $P_{0/R}, P_{2/0}, \xi_{0/R}$ or Q_ξ then depend on $\beta \equiv \Omega_{\rm m}^{0.6}/b_{\rm g}$, where $b_{\rm g}^2 = \xi_{\rm g}/\xi_{\rm m}$ is a monotonically decreasing function of σ_8 for fixed galaxy clustering (see Section 4.4). These measures scale with cosmological parameters as predicted by linear theory and the linear bias model (Kaiser 1987), even though these approximations do not provide an accurate description of anisotropy on most scales accessible to observations or to our simulations. One can estimate β by fitting $P_{0/R}, P_{2/0}$ or Q_ξ as a function of scale using our equations (16)–(18), or by measuring $\xi_{0/R}$ at $r \geqslant 10\,h^{-1}$ Mpc and correcting for the ~ 6 per cent bias of linear theory (see Fig. 12). The turnover scales in the fitting functions depend on the velocity bias $\alpha_{\rm v}$, but they can be measured directly from the anisotropy

ratios, so the β estimates themselves are largely independent of α_v.

The turnover scales can be used to break degeneracies in the parameter space, but the line-of-sight correlation function $\xi(r_\pi)$ at fixed, small r_σ provides a more direct measure of velocity distortions in the highly non-linear regime. In particular, for small r_σ the scale $r_{\xi/2}$ defined by $\xi(r_\sigma, r_{\xi/2}) = 0.5 \times \xi(r_\sigma, 0)$, quantifies the typical length of 'FOG', and hence the characteristic amplitude of pairwise velocity dispersions. At $r_\sigma \sim 0.1\,h^{-1}$ Mpc, where most pairs come from intermediate mass haloes, we find that $r_{\xi/2}$ depends on $\Omega_m \alpha_v^2$ with essentially no dependence on σ_8. At $r_\sigma \sim 1$–$5\,h^{-1}$ Mpc, $r_{\xi/2}$ has a significant dependence on σ_8 even at fixed β and α_v, with $\Delta \sigma_8 \sim 0.1$ corresponding to $\Delta r_{\xi/2} \sim 5$ per cent. Therefore, one can in principle use measurements of large-scale anisotropy and $\xi(r_\pi)$ at $r_\sigma \sim 0.1$–$5\,h^{-1}$ Mpc to separately determine the values of Ω_m, σ_8 and α_v. Alternatively, one can measure β and $\Omega_m \alpha_v^2$ as described above and adopt theoretical priors on α_v from hydrodynamic simulations of galaxy formation (e.g. Berlind et al. 2003), or combine redshift-space distortions with other observables that constrain different combinations of σ_8 and Ω_m. For example, galaxy–galaxy lensing measurements constrain $\sigma_8 \Omega_m$ (instead of $\sigma_8 \Omega_m^{0.6}$) from the ratio of the galaxy–mass correlation function to the galaxy autocorrelation function (Sheldon et al. 2004; see further discussion in Yoo et al. in press). The galaxy bispectrum can yield a direct estimate of σ_8 by determining the large-scale galaxy bias factor (Fry 1994; Verde et al. 2002). Cluster mass-to-light ratios offer additional cosmological constraints. HOD models with low values of σ_8 require more galaxies to occupy high-mass haloes, lowering the predicted M/L values of galaxy clusters (van den Bosch et al. 2003; Tinker et al. 2005).

Our blueprint has significant advantages relative to the linear–exponential model or the alternative fitting procedure of HC99. First, our approach is more accurate for a wide range of cosmological models (Figs 6 and 12). Averaging over both values of Γ used, our fitting function for $P_{0/R}$ yields β with an rms error of 1.6 per cent for the range of models presented. For the $P_{2/0}$ and Q_ξ diagnostics, the fitting functions yield rms errors of 4.1 and 3.9 per cent, respectively. Secondly, our approach makes use of the small-scale anisotropy as a tool for breaking parameter degeneracies, instead of treating the galaxy dispersion as a nuisance parameter. Constraints on σ_8 and α_v from these small-scale measures can be used to further improve the β estimate.

The fitting formulas presented here are designed to allow straightforward parameter estimation given measurements of $\xi(r_\sigma, r_\pi)$ and $P_Z(k, \mu)$. Alternatively, one can use simulations to calibrate a fully analytic description of redshift-space anisotropy, in which case one can fit data directly using Ω_m, σ_8 and α_v as the fitting parameters. We will develop such a model in Paper II; achieving the accuracy demanded by data sets like the SDSS and the 2dFGRS is not easy, but it is possible. The analytic method is more flexible than the fitting-formula approach, allowing one to take more complete advantage of information in $\xi(r_\sigma, r_\pi)$ or $P_Z(k, \mu)$. At the opposite extreme, one can circumvent analytic formulations entirely and fit data by directly populating haloes of N-body simulations and measuring anisotropy, using the Ω_m-scaling technique of this paper to improve efficiency. With large volume simulations that resolve the necessary halo masses, this method should achieve the highest accuracy because it fully describes non-linear halo clustering, and it can address corrections to the distant-observer approximation and other technical issues that are difficult to model analytically. In practice, it will probably be the best to use the fitting formulas or an analytic model to locate the most interesting regions of parameter

space, then use focused numerical simulations to check and refine estimates.

For the $\alpha_v = 0$ model, large-scale anisotropy measures agree reasonably with linear theory over a substantial range in scale. This result suggests that FOG compression plus linear theory is a viable alternative approach to estimating β. Assessing the systematic uncertainties of this method requires tests with realistic mock catalogues that quantify the ability of the FOG compression algorithm to correctly identify and compress true FOGs in galaxy survey data. Several studies have applied the FOG compression technique to find galaxy groups in the 2dFGRS (Zadivarez, Merhcan & Padilla 2003; Padilla et al. 2004; Yang et al. 2005). In the measurements of $\xi(r_\sigma, r_\pi)$ for these group catalogues, FOGs are nearly absent while the large-scale distortions are still detected.

There are several limitations to our blueprint. With two exceptions, we have assumed that central galaxies move with the centre of mass of the halo, i.e. $\alpha_{vc} = 0$. Changing α_{vc} to 0.2 makes minimal difference in both the large-scale measures and $r_{\xi/2}$. However, setting $\alpha_{vc} \approx 1$ makes a considerable difference. Current hydrodynamical simulations (Berlind et al. 2003) suggest $\alpha_{vc} \lesssim 0.2$ is a reasonable assumption, but the issue merits further investigation because of its significant impact on redshift-space anisotropy modelling. Analysis of SDSS galaxies shows that central-satellite galaxy pairs indeed have a narrower velocity spread than satellite–satellite pairs (McKay et al. in preparation). We have also assumed that α_v is independent of halo mass. This assumption should be adequate because most one-halo pairs come from a limited range of halo masses; low-mass haloes have no satellites and high-mass haloes are rare. To significantly alter our results, α_v would need to depend strongly on mass in the relatively narrow range $M_1/2$–$5\,M_1$, and even then its effect might be well represented by an average value. The weak mass dependence seen in the simulations analysed by Berlind et al. (2003) does not affect the results here, but the question again merits investigation in future hydrodynamic studies of galaxy formation. One can also test for mass dependence of α_v by comparing the predicted and observed scalings of group velocity dispersions with group richness.

The experiments illustrated in Fig. 7 show that changing the details of the HOD, or the assumption about spatial bias within haloes, has negligible impact on redshift-space distortions provided one matches the same real-space clustering. However, our investigation of these points is not exhaustive. Effects of changing α_{vc}, making α_v mass dependent, or changing HOD prescriptions while maintaining $\xi_R(r)$ can all be examined in more detail using the analytic model of Paper II.

The simulations presented in this work have less dynamic range than is ideal. At the largest scales, our numerical predictions are less precise than the measurement precision achievable with 2dFGRS or SDSS data, though not by a large factor. We have focused on predictions for luminosity-threshold galaxy samples with space density $5.6 \times 10^{-3}\,(h^{-1}\,\mathrm{Mpc})^{-3}$, corresponding roughly to $M_r < -20 + 5 \log h$. To make predictions or test fitting formulas for fainter galaxies, which occupy less massive haloes, one would need higher-resolution simulations but similar simulation volumes. To get precise results for more luminous galaxies that reside in rare, massive haloes, one would need larger simulation volumes, though the mass resolution required is lower. The analytic model described in Paper II can easily be applied to samples with different luminosity or colour selection and correspondingly different HODs, and it automatically extends to large scales. However, additional simulations will be needed to test the accuracy of the analytic model in these regimes.

The monopole-to-real-space ratios, $P_{0/R}$ and $\xi_{0/R}$, have smaller systematic errors as estimators of β than the quadrupole-to-monopole ratios $P_{2/0}$ and Q_ξ. However, we have not addressed the problem of estimating $\xi_R(r)$ or $P_R(k)$ from data. Techniques for estimating these quantities exist (e.g. Davis & Peebles 1983; Hamilton et al. 2000; Tegmark et al. 2004a; Zehavi et al. 2005), but we do not yet know whether they are accurate at the $\sim$1–2 per cent level required if they are not to contribute significantly to uncertainties in the estimates of β.

Despite these limitations, our results demonstrate that HOD modelling can substantially improve the accuracy and precision of redshift-space distortion analysis by replacing ad hoc extensions of linear perturbation theory with a complete, fully non-linear description of dark matter dynamics and galaxy bias. This level of sophistication is required to take full advantage of data provided by the 2dFGRS and SDSS. Precise cosmological constraints from galaxy clustering complement those from other cosmological observables like CMB anisotropy, gravitational lensing, the Lyman α forest, or Type Ia supernovae. They thus enhance the opportunity to detect departures from the simplest ΛCDM model, which could provide insight into the physics of dark energy or the origin of primordial fluctuations.

ACKNOWLEDGMENTS

REFERENCES

Abazajian A. et al., 2005, ApJ, 625, 613
Bean A. J., Ellis R. S., Shanks T., Efstathiou G., Peterson B. A., 1983, MNRAS, 205, 605
Benson A. J., 2001, MNRAS, 325, 1039
Benson A. J., Cole S., Frenk C. S., Baugh C. M., Lacey C. G., 2000, MRNAS, 311, 793
Berlind A. A., Weinberg D. H., 2002, ApJ, 575, 587
Berlind A. A., Narayanan V. K., Weinberg D. H., 2001, ApJ, 549, 688
Berlind A. A. et al., 2003, ApJ, 593, 1
Blanton M. R. et al., 2003, ApJ, 592, 819
Bullock J. S., Kolatt T. S., Sigad Y., Somerville R. S., Klypin A. A., Primack J. R., Dekel A., 2001, MNRAS, 321, 559
Cole S., Fisher K. B., Weinberg D. H., 1994, MNRAS, 267, 785
Cole S., Fisher K. B., Weinberg D. H., 1995, MNRAS, 275, 575
Colless M. et al., 2001, MNRAS, 328, 1039
Collister A. A., Lahav O., 2005, MNRAS, 361, 415
Cooray A., 2004, MNRAS, 348, 250
Cooray A., Sheth R. K., 2002, Phys. Rep., 372, 1
Davis M., Geller M. J., Huchra J., 1978, ApJ, 221, 1
Davis M., Peebles P. J. E., 1983, ApJ, 267, 465
Davis M., Efstathiou G., Frenk C. S., White S. D. M., 1985, ApJ, 292, 371
Diemand J., Moore B., Stadel J., 2004, MNRAS, 352, 535
Efstathiou G., Bond J. R., White S. D. M., 1992, MNRAS, 258, 1

Faltenbacher A., Kravtsov A. V., Nagai D., Gottlöber S., 2005, MNRAS, 358, 139
Fisher K. B., Nusser A., 1996, MNRAS, 279, L1
Fisher K. B., Davis M., Strauss M. A., Yahil A., Huchra J. P., 1994, MNRAS, 267, 927
Fry J. N., 1994, Phys. Rev. Lett., 73, 215
Ghigna S., Moore B., Governato F., Lake G., Quinn T., Stadel J., 2000, ApJ, 544, 616
Hamilton A. J. S., 1992, ApJ, 385, L5
Hamilton A. J. S., 1998, in Hamilton D., ed., The Evolving Universe. Kluwer, Dordrecht, p. 185
Hamilton A. J. S., Tegmark M., Padmanabhan N., 2000, MNRAS, 317, L23
Hatton S., Cole S., 1998, MNRAS, 296, 10
Hatton S., Cole S., 1999, MNRAS, 310, 1137 (HC99)
Hawkins E. et al., 2003, MNRAS, 346, 78
Hu W., Kravtsov A. V., 2003, ApJ, 584, 702
Jenkins A., Frenk C. S., White S. D. M., Colberg J. M., Cole S., Evrard A. E., Couchman H. M. P., Yoshida N., 2001, MNRAS, 321, 372
Jing Y. P., Mo H. J., Börner G., 1998, ApJ, 494, 1
Kaiser N., 1987, MNRAS, 227, 1
Kang X., Jing Y. P., Mo H. J., Börner G., 2002, MNRAS, 336, 892
Kauffmann G., Nusser A., Steinmetz M., 1997, MNRAS, 286, 795
Klypin A., Gottlöber S., Kravtsov A. V., Kohklov A. M., 1999, ApJ, 516, 530
Kravtsov A. V., Berlind A. A., Wechsler R. H., Klypin A. A., Gottlöber S., Allgood B., Primack J. R., 2004, ApJ, 609, 35
Kuhlen M., Strigari L. E., Zentner A. R., Bullock J. S., Primack J. R., 2005, MNRAS, 357, 387
Ma C., Fry J. N., 2000, ApJ, 543, 503
Magliocchette M., Porciani C., 2003, MNRAS, 346, 186
Melott A. L., 1983, ApJ, 264, 59
Mo H. J., Yang X., van den Bosch F. C., 2004, MNRAS, 349, 205
Nagai D., Kravtsov A. V., 2005, ApJ, 618, 557
Navarro J. F., Frenk C. S., White S. D. M., 1997, ApJ, 490, 493 (NFW)
Padilla N. D. et al., 2004, MNRAS, 352, 211
Park C., 1990, MNRAS, 242, 59
Park C., Vogeley M. S., Geller M. J., Huchra J. P., 1994, ApJ, 431, 569
Peacock J. A., Dodds S., 1994, MNRAS, 267, 1020
Peacock J. A., Smith R. E., 2000, MNRAS, 318, 1144
Peacock J. A. et al., 2001, Nat, 410, 169
Peebles P. J. E., 1976, ApJ, 205, L109
Peebles P. J. E., 1979, AJ, 84, 730
Percival W. J. et al., 2002, MNRAS, 337, 1068
Sargent W. L. W., Turner E. L., 1977, ApJ, 212 L3
Scoccimarro R., 2004, Phys. Rev. D, 70, 3007
Scoccimarro R., Sheth R. K., Hui L., Jain B., 2001, ApJ, 546, 20
Seljak U., 2000, MNRAS, 318, 203
Seljak U., 2001, MNRAS, 325, 1359
Seljak U., Zaldarriaga M., 1996, ApJ, 469, 437
Sheldon E. et al., 2004, AJ, 127, 2544
Sheth R. K., Diaferio A., 2001, MNRAS, 322, 901
Sheth R. K., Hui L., Diaferio A., Scoccimarro R., 2001, MNRAS, 325, 1288
Spergel D. N. et al., 2003, ApJ, 148, 175
Springel V., Yoshida N., White S. D. M., 2001, New Astron., 6, 79
Springel V., White S. D. M., Tormen G., Kauffmann G., 2004, MNRAS, 352, 726
Strauss M. A., Willick J. A., 1995, Phys. Rep., 261, 271
Strauss M. A. et al., 2002, AJ, 124, 1810
Tegmark M. et al., 2004a, ApJ, 606, 702
Tegmark M. et al., 2004b, Phys. Rev. D, 69, 103501
Tinker J. L., Weinberg D. H., Zheng Z., Zehavi I., 2005, ApJ, 631, 41
van den Bosch F. C., Yang X., Mo H. J., 2003, MNRAS, 345, 723
van den Bosch F. C., Norberg P., Mo H., Yang X., 2004, MNRAS, 352, 1302
Verde L. et al., 2002, MNRAS, 335, 432
White M., 2001, MNRAS, 321, 1
White M., Hernquist L., Springel V., 2001, ApJ, 550, L129
Yang X., Mo H. J., Jing Y. P., van den Bosch F. C., Chu X. Q., 2004, MNRAS, 350, 1153

Yang X., Mo H., van den Bosch F. C., Jing Y. P., 2005, MNRAS, 357, 608
Yoo J., Tinker J. L., Weinberg D. H., Zheng Z., Katz N., Davé R., ApJ, in press (astro-ph/0511580)
York D. et al., 2000, AJ, 120, 1579
Yoshikawa K., Taruya A., Jing Y. P., Suto Y., 2001, ApJ, 558, 520
Yoshikawa K., Jing Y. P., Börner G., 2003, ApJ, 590, 654
Zadivarez A., Merhcan M. E., Padilla N. D., 2003, MNRAS, 344, 247

Zehavi I. et al., 2004, ApJ, 608, 16
Zehavi I. et al., 2005, ApJ, 630, 1
Zheng Z., 2004, ApJ, 610, 61
Zheng Z., Tinker J. L., Weinberg D. H., Berlind A. A., 2002, ApJ, 575, 617
Zheng Z. et al., 2004, ApJ, 633, 791

This paper has been typeset from a TeX/LaTeX file prepared by the author.